Measurement of the Boltzmann Constant k_B Using a Quasi-Spherical Acoustic Resonator

**Laurent Pitre · Fernando Sparasci ·
Daniel Truong · Arnaud Guillou ·
Lara Risegari · Marc E. Himbert**

Abstract   There is currently great interest in the international metrological community for new accurate determinations of the Boltzmann constant k_B, with the prospect of a new definition of the unit of thermodynamic temperature, the kelvin. In fact, k_B relates the unit of energy (the joule) to the unit of the thermodynamic temperature (the kelvin). One of the most accurate ways to access the value of the Boltzmann constant is from measurements of the velocity of the sound in a noble gas. In the method described here, the experimental determination has been performed in a closed quasi-spherical cavity. To improve the accuracy, all the parameters in the experiment (purity of the gas, static pressure, temperature, exact shape of the cavity monitored by EM microwaves, etc.) have to be carefully controlled. Correction terms have been computed using carefully validated theoretical models, and applied to the acoustic and microwave signals. We report on two sets of isothermal acoustic measurements yielding the value $k_B = 1.380\,647\,74(171) \times 10^{-23}$ J·K^{-1} with a relative standard uncertainty of 1.24 parts in 10^6. This value lies 1.9 parts in 10^6 below the 2006 CODATA value (Mohr et al., Rev. Mod. Phys. **80**, 633 (2008)), but, according to the uncertainties, remains consistent with it.

L. Pitre (✉) · F. Sparasci · D. Truong · A. Guillou · L. Risegari · M. E. Himbert
Laboratoire Commun de Métrologie LNE—Cnam (LCM), 61 rue du Landy,
93210 La Plaine Saint-Denis, France
e-mail: pitre@cnam.fr

1 Introduction

The new determination of the Boltzmann constant k_B reported here is based on the same principles as in the acoustic experiment of Moldover et al. [1], performed at NIST in 1988, which led to the most accurate determination of the universal gas constant R, and the Boltzmann constant, up to now. However, several fundamental modifications and improvements have been made in this new experiment to measure and control the parameters that influence the measurement of k_B [2,3].

The aim of this new experiment is to obtain a determination of k_B with an improved accuracy, necessary to set-up a new definition of the kelvin based on this fundamental constant, instead of the temperature of the triple point of water [4,5]. The idea is to determine R and k_B from measurements of the speed of sound c_a in a monatomic gas sample [1,6].

In the specific experiment performed, the Boltzmann constant is determined from a series of speed-of-sound measurements made in a 0.5 L quasi-spherical cavity made of copper, at different pressures, along an isotherm close to the temperature of the triple point of water $T_{TPW} = 273.16$ K.

These measurements are then polynomial functions of the pressure, to obtain $c_a(0\,Pa, 273.16\,K)$ and k_B from the relation,

$$k_B = \frac{R}{N_A} = \frac{A_r(Ar) \cdot M_u}{5/3 T_{TPW} N_A} \lim_{p \to 0} {}^* c_a^2 (p, T_{TPW}) \tag{1.1}$$

where $c_a^2 (p, T_{TPW})$ is the square of the speed of sound at a pressure p and at the temperature of the triple point of water, T_{TPW}. $A_r(Ar)$ is the relative atomic mass of argon (alternatively, we can use helium, and this term becomes $A_r({}^4He)$), M_u is the molar mass constant, N_A is the Avogadro constant, and the factor 5/3 is the ratio $\gamma = C_p / C_V$ of the specific heat capacities for dilute monatomic gases. The term $\lim_{p \to 0} (c_a^2 (p, T_{TPW}))$ indicates that we estimate the terms independent of the pressure in $c_a^2 (p, T_{TPW})$.

In this work we have redetermined R and k_B with the following results:

- $R = 8.314\,456\,4(103)$ J $\cdot$ mol^{-1} $\cdot$ K^{-1}, i.e., with a relative standard uncertainty of 1.24 parts in 10^6;
- $k_B = 1.380\,647\,74(171) \times 10^{-23}$ J $\cdot$ K^{-1}, i.e., with a relative standard uncertainty of 1.24 parts in 10^6.

For the calculation of k_B from R, we have used the 2006 CODATA recommended value of the Avogadro constant $N_A = 6.022\,141\,79(30) \times 10^{23}$ mol^{-1} [6].

The present value of k_B is compared in Fig. 1 with other recent determinations of the Boltzmann constant. Our value is consistent with these new values and with the CODATA value, which is mainly based on the results of the speed of sound measurements in argon carried out in 1988 at NIST by Moldover et al. [1]. The 2006 CODATA recommended value for k_B was $1.380\,650\,4(24) \times 10^{-23}$ J $\cdot$ K^{-1} The summary of the uncertainty contributions in our redetermination of the Boltzmann constant is reported in Table 1.
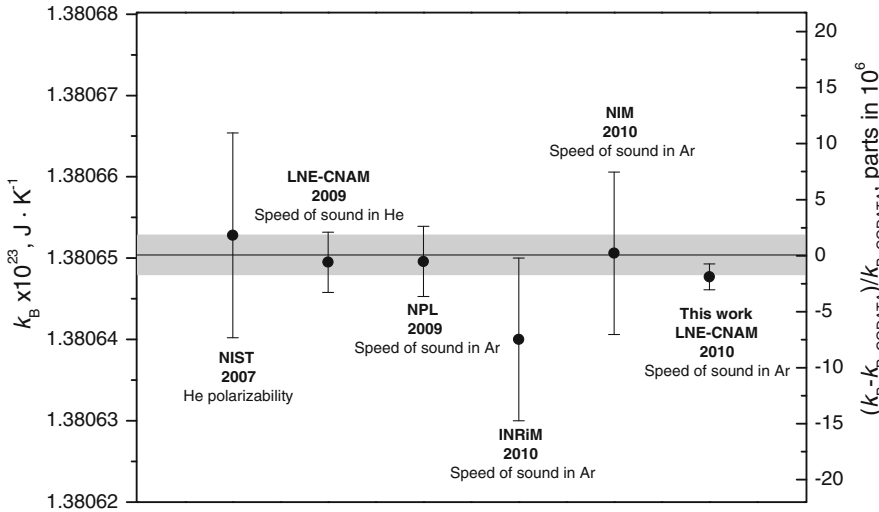
Fig. 1 Comparison of the recent determinations of k_B with the 2006 CODATA recommended value k_{B_CODATA} [6]. The *shaded area* spans u (k_{B_CODATA}). The determinations of 2009 by Pitre et al. [7] and by Sutton et al. [2], and of 2010 by Gavioso et al. [8] were, respectively, obtained at LCM (LNE-CNAM), at NPL, and at INRiM, by measuring the speed of sound in He and Ar with quasi-spherical resonators. The value from Zhang et al. [9] was obtained at NIM with a cylindrical acoustic resonator

Table 1 Overall relative standard uncertainty on the Boltzmann constant determination performed in argon at LCM (LNE-CNAM)

Term	Uncertainty contribution on k_B in parts in 10^6	Note
Temperature measurements	0.30	Section 3
Volume EM measurements	0.57	Section 4
Acoustic measurements	0.84	Section 5
Molar mass and gas purity	0.60	Section 6
Repeatability over two isotherms	0.25	Difference between two different runs (May and July 2009)
Total	**1.24**	**Square root of the sum of squares**

For an accurate determination of the speed of sound in a dilute gas, methods involving the measurement of the resonance frequencies of standing waves in cavities of simple geometry remain unsurpassed. For acoustic fields of a high quality factor, non-degenerate modes of such cavities are experimentally well-defined, theoretically well-understood [10,11], and can be achieved with a mechanically simple apparatus.

The speed of sound in a gas can be determined experimentally by measuring acoustic resonances in a perfect spherical cavity of known radius. The speed of sound is related to the resonance frequencies f_{nl}^A, to the corrections Δf_{nl}^A taking into account the effects of the cavity and of the nonideality of the gas, and to the eigenvalues Z_{nl}^A

for the wavenumbers (n, l) in the acoustic cavity. In the particular case of a spherical cavity of radius a, we have

$$c_a(p, T_{\text{TPW}}) = \frac{f_{nl}^{\text{A}}(p, T_{\text{TPW}}) + \Delta f_{nl}^{\text{A}}(p, T_{\text{TPW}})}{Z_{nl}^{\text{A}}} 2\pi a(p, T_{\text{TPW}}) \qquad (1.2)$$

A microwave technique can be used in combination with acoustic measurements to determine the cavity dimensions as a function of temperature and pressure [7,12]. This experimental technique allows determination of the thermal expansion of spherical cavities in acoustic thermometry, and has successfully been applied in several experiments, as shown in [13–18].

The accuracy in the determination of microwave eigenfrequencies, used to determine the cavity dimensions, can be improved removing the degeneracy associated with the microwave eigenfunctions, and adopting a quasi-spherical geometry for the shape of the resonant cavity, and in particular, that of a triaxial ellipsoid [19,20].

For such geometry, a theoretical calculation of the second-order corrections of microwave eigenvalues has only recently been completed [21], and found to be in outstanding agreement with the results of experiments [22].

Acoustic and microwave measurements were carried out simultaneously. From the microwave data, we determined $a(p, T_{\text{TPW}})$, the average radius of the cavity resonator as a function of the pressure at T_{TPW}. This quantity was used to transform the measured acoustic resonance frequencies f^{A} into the speed-of-sound values c_a used for the determination of k_{B} with the relation:

$$\begin{aligned}
k_{\text{B}} &= \left\langle \frac{3}{5} \frac{m}{T_{\text{TPW}}} \lim_{p \to 0}{}^* \left(\frac{2\pi a}{Z_{nl}^{\text{A}}}\right)^2 \left(\left\langle f_{nl}^{\text{A}} + \Delta f_{nl}^{\text{A}} \right\rangle\right)^2 \right\rangle \qquad (1.3)\\
&= \left\langle \frac{3}{5} \frac{m c_0^2}{T_{\text{TPW}}} \left(\frac{Z_{nl}^{\text{EM}}}{Z_{nl}^{\text{A}}}\right)^2 \lim_{p \to 0}{}^* \left(\frac{\left\langle f_{nl}^{\text{A}} + \Delta f_{nl}^{\text{A}} \right\rangle}{\left\langle f_{nl}^{\text{EM}} + \Delta f_{nl}^{\text{EM}} \right\rangle}\right)^2 \right\rangle
\end{aligned}$$

where m is the atomic mass of the gas, c_0 is the speed of light in vacuum, Z_{nl}^{EM} and Z_{nl}^{A} are the eigenvalues of the quasi-sphere's (n, l)-th modes, for electromagnetic and acoustic waves, respectively. f_{nl}^{EM} and f_{nl}^{A} are, respectively, the measured electromagnetic and acoustic resonance frequencies, and $\Delta f_{nl}^{\text{EM}}$ and Δf_{nl}^{A} are corrections from theory. These corrections are explained in Sects. 4 and 5 and take into account the effects listed in [2]. $\langle \cdot \rangle$ is the average operator.

Table 1 lists the different uncertainty contributions to the measurement of k_{B}. Each element is related to the different quantities measured in Eq. 1.3 and is described in detail in the next sections of this article.

The main improvements with respect to the previous determination in [1] come from temperature measurements and the molar mass of gas measurements. The most innovative technique is the measurement of the volume of the resonator with microwaves. The nature of its uncertainties is completely different from that of the pycnometry used in [1]. Pycnometry in [1] was based on measurements of the density of mercury and

the assumption that the density did not change during storage. In contrast, the microwave technique requires an accurate model involving the geometry of the resonator, perturbations from antennas, and the penetration of the microwaves into the copper shell. Finally, this new determination of the Boltzmann constant is linked to the newly refined definition of the triple point of water taking into account the influence of the isotopic composition.

The structure of this article is the following: we start with a description of the experimental apparatus and procedures in Sect. 2; we describe the techniques used to perform temperature measurements in Sect. 3; we describe the procedure used to determine the internal volume of the resonator in Sect. 4; in Sect. 5, we explain the steps used to calculate the value of k_B with acoustic measurement and we describe the data analysis carried out with two independent isotherms; in Sect. 6 we consider the problem of purity of the gas; and in Sect. 7 we analyze the budget of uncertainties for our determination of k_B.

2 Mechanical Design

In this section, we describe our quasi-spherical resonator named BCU3. The description commences with the shapes of the hemispheres, the plugs, and fixtures. We continue with the fabrication process and dimensional measurements. We discuss the assembly of the hemispheres. After this, we describe the thermostat and the temperature-controlled bath.

2.1 Resonator

The BCU3 resonator is assembled from two copper hemispheres (Cu-ETP copper, ISO norm). We call the upper hemisphere NORTH and the lower hemisphere SOUTH where "upper" and "lower" refer to the assembled sphere when it is supported within the thermostat. We describe first the inner shape and then the outer shape.

2.1.1 Inner Shape

BCU3 is an acoustic resonator and an electromagnetic resonator as well. To lift the degeneracy of the electromagnetic resonances (see also Sect. 2.4), the inner shape is designed to be a triaxial ellipsoid defined by

$$\frac{x^2}{a^2} + \frac{y^2}{a^2(1+\varepsilon_2)^2} + \frac{z^2}{a^2(1+\varepsilon_1)^2} = 1 \tag{2.1}$$

with $a = 49.950$ mm, $\varepsilon_1 = 0.001$, and $\varepsilon_2 = 0.0005$. For practical purposes, we transpose this equation into the three radii along the axis of our reference system: $a_x = 49.950$ mm, $a_y = 49.975$ mm, and $a_z = 50.000$ mm. Figure 2 shows the reference system and the associated radii. Each axis defines a symmetry plane for the inner shape. The three keyways cutting the equatorial plane facilitate quick identification of the reference system on the real hemispheres.

Fig. 2 Definition of the
reference system and local radii
a_x, a_y, and a_z of the inner
ellipsoidal shape
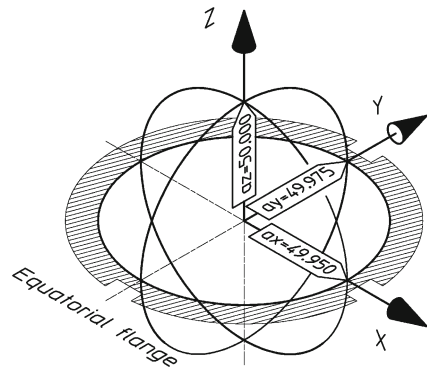
2.1.2 Outer Shape

Figure 3 is a cross section of the assembled sphere. The shell surrounding the cavity
was designed to closely approximate a uniform spherical shell with a 10 mm thick
wall. The NORTH outer surface is mainly spherical with a 60 mm radius. At the equa-
tor, a flange of 120 mm outer diameter is cut by three keyways which are used to align
the hemispheres. A vertical boss at the pole is used for clamping the sphere with good
thermal contact with the thermostat (see also Sect. 2.5). Two horizontal bosses mid-
way between the equator and the north pole accommodate housings for capsule-type
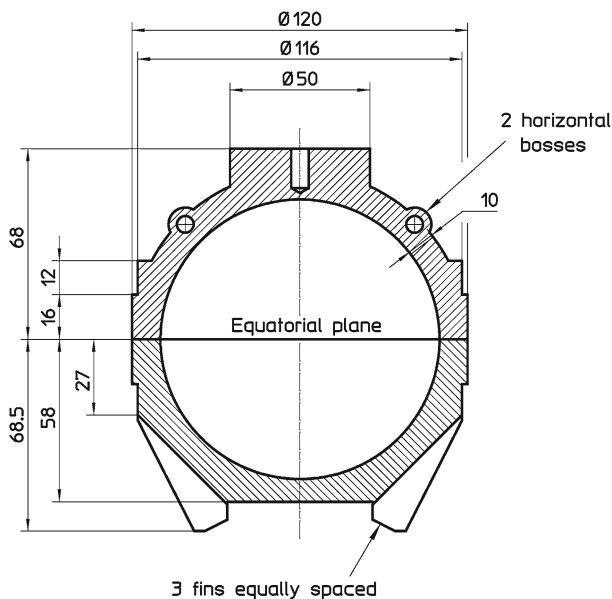thermometers.

Fig. 3 Cut view giving the dimensions (in mm) of the outer surfaces. Contrary to the drawing, the bosses
and fins were not in the same cross section

The SOUTH outer surface is cylindrical near the equator and conical over a third of the height. Three fins equally spaced are located to give maximum clearance to the plugs and can accommodate three capsule-type thermometers inside.

2.1.3 Ports and Plugs

Two acoustic transducers were used to measure acoustic resonance frequencies; two microwave antennas were used to measure microwave resonance frequencies; and two ducts were used to flow gas inside the sphere. Following the recommendation of Mehl et al. [19], the angular positions (θ, φ) of the microphones were chosen for the best possible separation of the (0, 2) acoustic mode from the nearby (3,1) mode. The first microphone was located at the pole $(\pi/2, 0)$ and the second microphone was located at the angle 39.2° $(\pi/2, \arccos\sqrt{3/5})$. As shown in Fig. 4, the (0, 2) mode was very well resolved from the neighboring (3, 1) acoustic mode.

Six conical ports were drilled through the resonator walls, two in NORTH, and four in SOUTH. Figure 5 displays the shape and position of each plug. Except for Microphone 2, the axes of all the ports are at an angle of 45° with respect to the equatorial plane.

The resonator is provided with two sets of taper plugs. One is drilled to accommodate the acoustic transducers, antennas, and gas inlet and outlet tubes. The other set includes blank plugs that were installed in the resonator during the machining process. They provided a continuous inner surface that facilitated performing shape
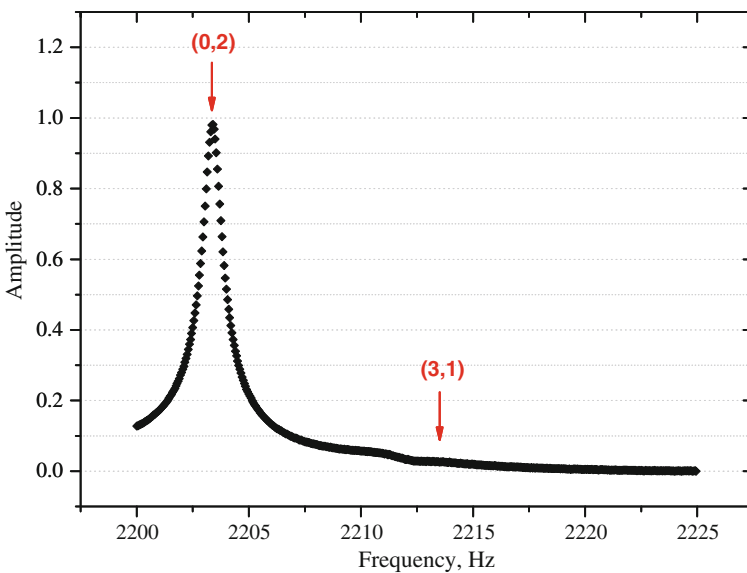

Fig. 4 Separation of (0, 2) and (3, 1) acoustic modes, measured in argon at 273 K and 0.1 MPa. Plot shows the relative amplitude of the acoustic pressure as a function of the frequency. *Arrows* show the resonance frequencies
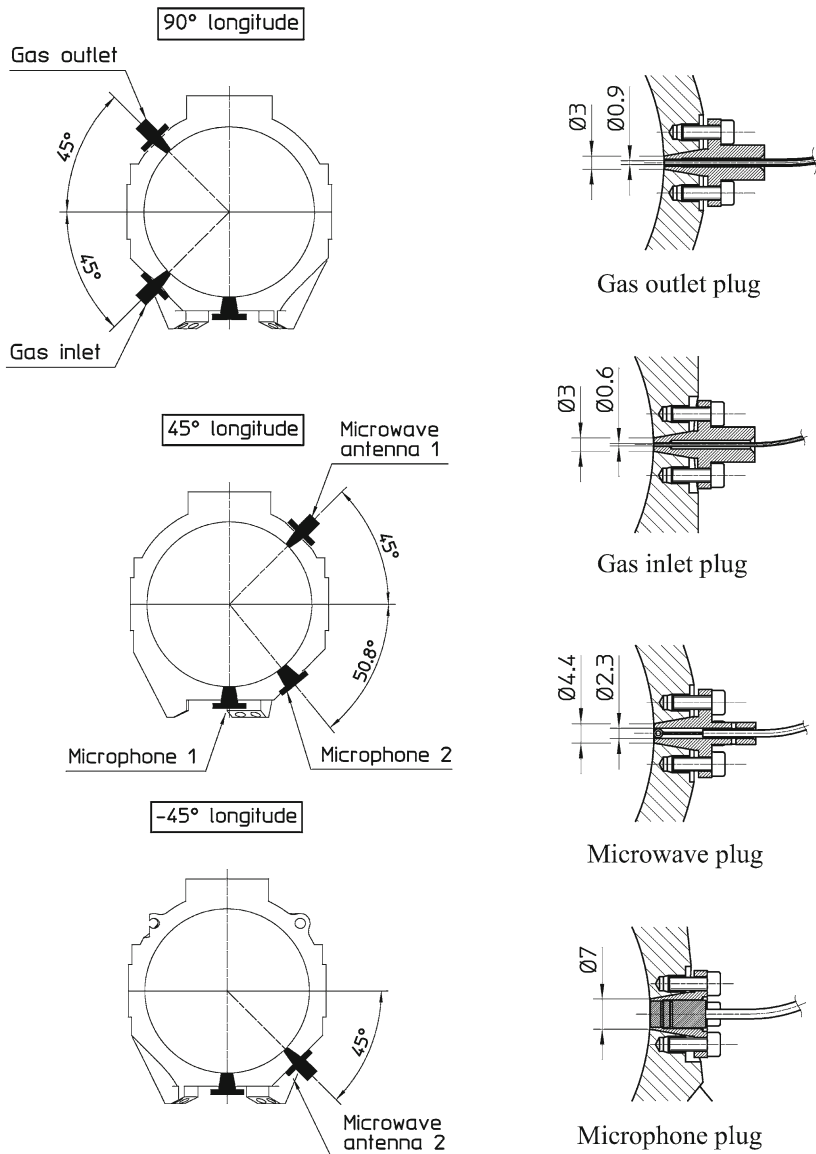
Fig. 5 Cross sections showing the locations and designs of the plugs. The spherical profile is shown in *thin solid lines*. The dimensions for the end diameters of the taper plugs, the diameters of the holes opening inside the cavity, and the inner diameter for the tubes, are all in mm

measurements with a coordinate measuring machine (CMM), and volume measurements with microwave resonances before beginning the acoustic measurements.

Each microphone plug accommodated a Brüel & Kjaer 1/4 inch (6.35 mm) condenser microphone. The outer diameter of each plug was carefully adjusted to place the membrane of the microphone flush with the interior surface of the resonator. Each microwave plug accommodated an antenna fabricated from the bare end of a coaxial

cable. Each gas plug embedded an electroformed nickel tube having one extremity glued flush with the internal surface of the plug. The inner diameters of the inlet and outlet tubes were 0.5 mm and 0.76 mm, respectively. We used Lesker® KL-320 K vacuum epoxy glue to seal the tubes in their plugs and to fill the cavity around the microwave antennas.

2.1.4 Clamp

The hemispheres were bolted together with twelve M5 screws. The plugs were clamped with four M3 screws. All the screws were tightened to a torque of 0.45 N · m. At the top of the sphere, a custom-made sliding nut with a right/left-hand M6 screw was used to fasten the assembled sphere to the thermostat head after all the wiring and tubes were connected. All of the threaded holes were equipped with Helicoil® inserts.

2.2 Fabrication

Prior to machining, the copper billet was annealed to relax stresses induced in the material by the rolling process. The heat treatment consisted of heating the copper to 250 °C and letting it cool very slowly. When the conventional machining operations were completed, the hemispheres were annealed a second time to relax stresses from the rough machining. The final fabrication step was precision diamond turning.

After the conventional machining was completed, the outer surfaces of the hemispheres had their final dimensions and the inner surfaces of the hemispheres were 1.5 mm from their final dimensions. The ports for the plugs had rough tapers. We finished the surfaces of the ports by grinding them with a conical hand tool coated with an abrasive paste.

The finishing operations were conducted with a Moore ultra-precision diamond-turning lathe[1]. These included diamond turning the inner surfaces, the equatorial plane, the outer cylinder, and plug tapers. During these operations, each hemisphere was held by the smaller cylindrical surface behind the equatorial flange (Fig. 3). The inner surface, the equatorial plane, and outer diameter of the flange were machined together. Therefore, these surfaces are accurately coaxial. Prior to the final inside cut, we used a SIP-Geneva length measurement machine to measure the equatorial radii. The resulting corrections were programmed into the diamond-turning lathe. The final cut removed a 3 μm thick layer of copper. Using these procedures, the deviation expected from the designed form was less than 3 μm peak-to-valley with a linear averaged roughness profile ($Ra = 2$ nm), which corresponded to a mirror finish.

The tapered plugs for the antennas, ducts, and microphones were also diamond-turned to achieve optimal contact with the ports. The inner surfaces of the blank plugs were diamond-turned while the plugs were in place in the hemisphere. The diamond turning of the drilled plugs took place separately using a specific holder. The shape of their ends was spherical with a radius close to 50 mm to approximate the ellipsoidal

---

[1] SAVIMEX, Parc d'Activité des Bois de Grasse, 1 avenue Louison Bobet, BP 85262-06131 Grasse cedex, France.

inner surface. Each plug was cut to the right length according to its location on the surface. Burrs were avoided by using a cutting trajectory that started from the flange, continued along the conical shape, and ended with the spherical shape, from the outer diameter to the center.

2.3 Dimensional Measurements

The primary motivation for making dimensional measurements of our resonator was to check that the manufactured parts conformed to our design. We used a coordinate measurement machine of type ZEISS UPMC 550 CMM at NPL [23] for mapping the inner surface and the flange. During measurements, the hemispheres sat on the CMM table without the help of a holder. We were particularly concerned that the inner surfaces of NORTH and SOUTH formed a continuous surface when the hemispheres were assembled. It was critical that the assembled cavity contain no micrometer-sized edges. We could accept an inner surface that deviated from the theoretical form as long as the deviations were smooth functions of the angular coordinates (θ, φ). Then, the actual shape could be determined by fitting CMM data to spherical harmonics.

The CMM technique is so accurate that we used it to determine the volume, independent of the microwave technique [23]. Elsewhere, we provide a detailed report of how we used BCU3 to optimize the CMM technique for volume measurements [23]. A spherical harmonic regression to the CMM data for BCU3 indicated that the data had uncertainties on the order of 100 nm. This led to an uncertainty of 2 parts in 10^6 for the determination of the equivalent spherical radius a_{eq}. Table 2 compares the results of the CMM determination of a_{eq} with the results of the microwave determination of a_{eq}.

The disagreement between the two measurements can be explained by the change of the volume as the bolts were tightened. One of the hypothesis is that when the two hemisphere are assembled and bolted, the pressure of the bolts may compress the hemispheres reducing the volume perceived by the electromagnetic field. This was first suggested by Albo [24], and it was confirmed by Underwood et al. [25]. When we assemble resonators in the future, we will use the microwave technique to measure the changes in volume while we gradually tighten the bolts.

2.4 Assembly of the Resonator

We experimented with two different assembly procedures. In the first, presented in Sect. 2.4.1, we used vertical cylinders and we made some microwave measurements

Table 2 Equivalent radii from CMM ($a_{\text{eq}}^{\text{CMM}}$) and microwave measurements ($a_{\text{eq}}^{\text{MW}}$)

$a_{\text{eq}}^{\text{CMM}}$ (μm)	Uncertainty (μm)	$a_{\text{eq}}^{\text{MW}}$ (μm)	Uncertainty (μm)
49975.383	0.1	49975.095	0.014

in this configuration. Then, we reopened the sphere and performed a second assembly using a plastic ring that we describe in Sect. 2.4.2.

2.4.1 Visual Alignment

The first assembly used a steel base plate for horizontal reference and two vertical cylinders for vertical alignment. All contact surfaces of the cylinders were ground. SOUTH was placed on the table in contact with the two cylinders. Then NORTH was put in contact with the cylinders and gently lowered towards the equatorial plane of SOUTH. A plastic guide pin maintained the angular alignment of the two hemispheres during this phase. When the contact between all the surfaces was realized, and was optically checked, the hemispheres were bolted together. Figure 6 shows the setup.

2.4.2 Alignment with Ring

The second assembly procedure used an alignment ring. We used a ring made of Ertalyte®, for which the thermal expansion (60×10^{-6} m · m^{-1} · K^{-1}) is more than three times that of copper (17×10^{-6} m · m^{-1} · K^{-1}). The ring was first inserted on SOUTH's equatorial cylinder. The temperature of the room was cooled from $16\,°C$ to $12\,°C$ until the ring was clamped onto the hemisphere. Then, room temperature was slightly raised to $16\,°C$. We waited until it was possible to insert NORTH's cylinder inside the ring. As soon as this point was reached, we lowered NORTH inside the ring, until it made contact with the equatorial plane of SOUTH. The assembly was then cooled to $12\,°C$ to align the two hemispheres without any residual gap. Finally, the hemispheres were bolted together. Figure 6 shows this assembly too.

The reproducibility of the microwave measurements of ε_1 and ε_2 made after the two alignments was within $0.1\,\mu$m. We concluded that both methods were accurate enough to correctly align the sphere.

Evidence that the final alignment was satisfactory is provided by Fig. 7 which displays the TM11 microwave triplet. The amplitude of the first two peaks is half of the
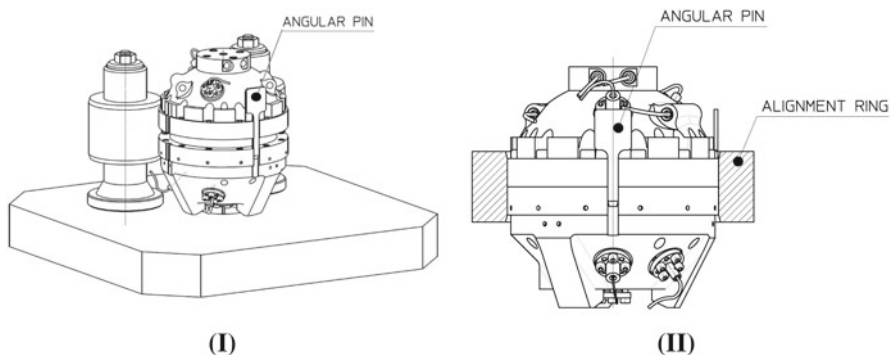

Fig. 6 (I) 3D view of the assembly with *two cylinders*. Sphere is shown partially open. (II) Cut view of the assembly with an *alignment ring*
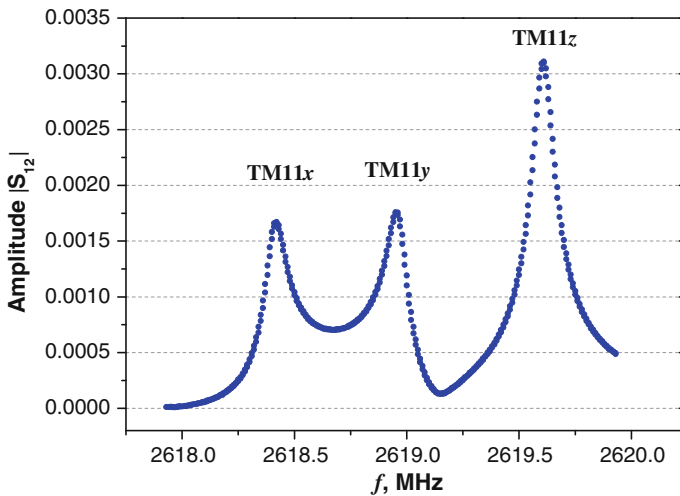
Fig. 7 Typical TM11 microwave resonances with straight antennas. The plot shows the expected amplitude ratios of 1/2 between the TM11x and TM11z resonances and between the TM11y and TM11z resonances

amplitude of the third peak. This is expected for a one-piece ellipsoidal cavity, given the positions of the antennas with respect to the equatorial seam.

2.5 Thermostat and Temperature-Controlled Bath

For the measurements using BCU3, the thermostat was designed to resemble a low-temperature cryostat (similar to those already used in this laboratory [16]). It was composed of a vacuum chamber—in which conductive and convective heat transfers are minimized—and it was equipped with a thermal shield to reduce radiative heat transfer. The thermostat was immersed in a temperature-controlled liquid bath maintained at a temperature close to that of the triple point of water. Because of the vacuum insulation and the radiation shield, bath oscillations of several millikelvins did not affect the thermal stability of the acoustic resonator.

The thermostat, represented in Fig. 8, consisted of a cylindrical stainless steel vacuum can joined to an upper stainless steel flange with an indium gasket. It was immersed in a temperature-controlled liquid bath. The center of the upper flange was connected to an 8 mm diameter tube that was led to the vacuum pump and contained a 1 m long stainless steel corrugated hose, enclosing electrical wires, coaxial cables, and the capillary used to supply the gas to the acoustic resonator. The exhaust gas flowed from the resonator through the corrugated tube up to the external vent. Thus, the exhaust gas flow exchanged heat with the incoming gas and contributed to the heat-sinking of the cables.

In order to shield the resonator from the temperature oscillations of the liquid bath, we hung the apparatus inside the vacuum can using a weak thermal link composed of three stainless steel tubes 80 mm high, 6 mm outer diameter, and 0.2 mm thick. The link connected the stainless steel lid of the pressure vessel to a gold-plated, copper
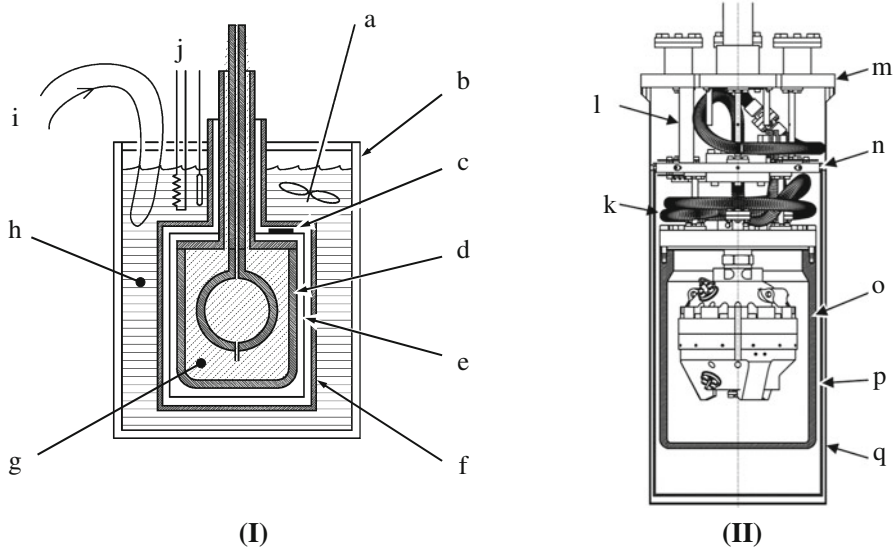
(I) **(II)**

Fig. 8 (I) Schematic diagram of the sphere in the thermostat: *a* stirring propeller, *b* Dewar, *c* heater, *d* pressure vessel, *e* radiation shield, *f* vacuum vessel, *g* Ar or He gas, *h* water + ethylene glycol bath, *i* cooler, *j* heater. (II) Cut view of the thermostat head in bath: *k* corrugated hose thermalizing tubes and wires, *l* thermal link, *m* vacuum vessel lid, *n* thermal shield top plate, *o* gold-plated copper pressure vessel, *p* gold-plated copper thermal shield, and *q* stainless steel vacuum vessel

flange that acted as the top of the radiation shield. This copper flange was temperature-controlled with a heater and ten $100\,\Omega$ platinum resistance thermometers (Pt100) uniformly distributed over its upper face. A gold-plated copper, cylindrical, thermal shield was screwed to the copper flange. To cool the resonator quickly, the weak thermal link was short-circuited by a removable copper bar.

The copper flange served as a heat sink for the cables and the gas inlet tube that led from the lab to the resonator. To improve the heat sinking, the flange had a central hole enclosed by two copper caps, one on the top and the other on the bottom. The caps were screwed and sealed to the flange with an indium gasket. Thus, the caps enclosed a small, sealed, gas-filled chamber. The corrugated hose coming from the upper part of the cryostat was welded to the upper cap. A second corrugated tube was welded to the lower cap; this tube was connected to the pressure vessel. The cables and the gas inlet tube were heat sunk as they passed through each cap and by the gas in the chamber.

The pressure vessel was a thick-walled, gold-plated, copper cylinder (6 mm thick, 226 mm high, 158 mm outer diameter), screwed onto a gold-plated copper flange and sealed with an indium gasket. The flange of the pressure vessel was suspended from the flange of the heat shield by a second weak thermal link consisting of three stainless-steel tubes (60 mm high, 6 mm outer diameter, 0.2 mm thick). During normal operation, the "exhaust" gas flowed out of the resonator, into the pressure vessel surrounding it, and through the corrugated tubes to a pump. As the experimental conditions were changed, the pressure inside the pressure vessel varied from near-vacuum up to

0.7 MPa while the outside of the vessel was always under vacuum. To avoid creating pressure-dependent temperature gradients, we did not thermostat the pressure vessel.

The acoustic resonator was suspended from the lid of the pressure vessel by a copper rod that had a right-hand thread at one end and a left-hand thread at the other end. The threaded rod enabled us to mount the resonator without rotating it, thereby avoiding strains on the wires, coaxial cables, and gas-filled capillaries.

The temperature of the acoustic resonator was measured by four calibrated 25 Ω capsule-type standard platinum resistance thermometers (CSPRTs), installed in four of the thermometer housings machined into the resonator's shell. They were located on the top and at the bottom of the resonator, in order to measure possible temperature gradients. We note that the thermometers were in contact with the gas inside the pressure vessel; therefore, they were exposed to pressures up to 0.7 MPa. Although a heater was installed on the resonator, we decided to not use it to avoid generating thermal gradients in the shell. Thus, the resonator's temperature was not directly controlled; however, it was thermally linked to the pressure vessel by the threaded support rod, cables, gas capillaries, and the gas inside the pressure vessel that surrounded the resonator. In some experiments, a custom-made preamplifier located at the bottom of the resonator was used to amplify the signal of the receiving microphone. This amplifier dissipated approximately 70 μW while it was operating.

3 Temperature Measurements

Acoustic measurements for the determination of the Boltzmann constant are carried out at the temperature of the triple point of water T_{TPW} because, under the International System of Units, T_{TPW} defines the kelvin and is the only temperature with zero uncertainty. Because it is impossible to install the acoustic resonator inside a TPW cell, the acoustic resonator was installed in a temperature-controlled thermostat, operating at temperatures near T_{TPW}. The acoustic resonator has to be kept in isothermal conditions, i.e., thermal gradients over its surface have to be minimized. Therefore, temperature drifts have to be small enough that gradients generated by them are negligible. In Sect. 2.5, we described the thermostat that met these criteria. Here, we describe how the temperature of the thermostat was traced to the T_{TPW} using stable, calibrated thermometers.

The following sections describe how the thermometers are calibrated and show the results of temperature measurements made under different conditions. We investigate thermal gradients on the resonator shell and provide an uncertainty budget for the temperature measurements.

3.1 Thermometers and Calibration at the T_{TPW}

The resonator was equipped with four, calibrated, 25 Ω CSPRTs. Each thermometer was purchased from a different manufacturer to minimize the risk of introducing a bias resulting from some unknown feature of a specific type of CSPRT.

The thermometers were the following:

Fig. 9 Schematic diagram of the positions of the thermometers on the resonator
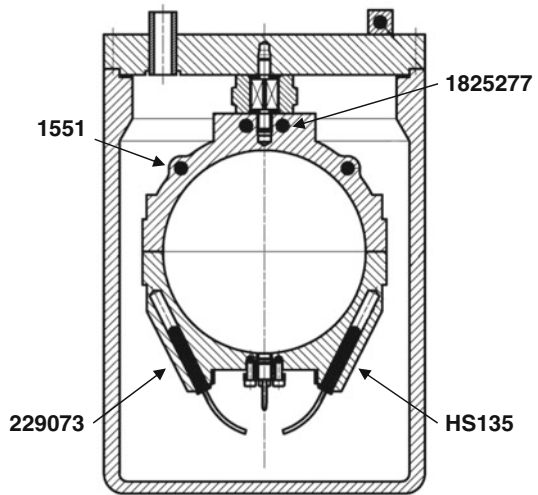
- Rosemount Model 162D, s.n. 1551;
- Leeds & Northrup, s.n. 1825277;
- Hart Scientific Model 5686, s.n. HS135;
- Tinsley Model 5187L, s.n. 229073.

The CSPRTs were embedded in different positions within the resonator's shell to measure its average temperature and to evaluate possible temperature gradients. Figure 9 shows the location of the four CSPRTs on the resonator.

3.1.1 Experimental Setup for Calibration and Measurement Configuration

All four CSPRTs were calibrated at T_{TPW}. These calibrations were carried out in a classical glass TPW cell [26]—which is designed to perform calibrations of long-stem platinum resistance thermometers—by adapting the CSPRTs so as they can fit inside the thermometric well. Two different assemblies were tested in several measurement configurations, in order to evaluate how the measurements uncertainties are affected.

In the first assembly, each CSPRT was fixed to a thin stainless steel capillary (length 500 mm, external diameter 2.3 mm, thickness 0.2 mm), and was immersed in an electrical insulating oil that partially filled the thermometric well and improved the thermal contact between the thermometer and the locations where the three water phases coexisted. The electrical wires passed inside the capillary, and the oil filling the thermometric well served as a heat sink for them. Both the small cross section of the capillary and the oil immersion reduced the heat brought from the room into the well of the TPW cell. The main advantage of this assembly was its simplicity; however, care had to be taken to avoid mechanical shocks to the thermometer and to avoid water vapor condensation on the thermometer's seal, where the leads are not electrically insulated. Condensed water vapor generates spurious impedances that can alter the measured resistance.

In the second assembly, the thermometer was installed in a water-tight copper sheath. The upper part of the sheath had been welded to a thin stainless steel capillary that surrounded the electrical wires. The capillary and the sheath were filled with dry gas, in order to prevent water vapor condensation on the thermometer's leads. The wires were thermally anchored inside the sheath. The advantages of this assembly are the protection of the thermometer against mechanical shocks and the possibility of calibrating the thermometer while the well is filled with pure water, as is done for long-stem thermometers. The main disadvantage is that, considering the high mass of the assembly compared with that of the thermometer, the assembly must be pre-cooled to a temperature near T_{TPW} prior to insertion into the well to avoid excessive alterations in the ice mantle of the TPW cell.

Several experiments were realized to characterize the performances of both assemblies. Measurements were performed using two AC resistance bridges (ASL Model F18, s.n. 008661/02 and Model F18 low current s.n. 011383/02), a calibrated standard resistor $R_{\text{S}} = 25.000\,016\,2(65)\,\Omega$ (Tinsley Model 5685A, s.n. 873715) and two calibrated long-stem standard platinum resistance thermometers (SPRTs) for additional checks. The TPW cell (Hart Model 5901, s.n. 1422) was part of the batch of cells composing the French TPW national standard, and the relationship between its temperature and T_{TPW} was given by

$$T_{\text{TPW}} = T_{\text{HS1422}} + \delta T_{\text{hydrostatic}} + \delta T_{\text{isotopic}} \\ + \delta T_{\text{batch}} + \delta T_{\text{purity}} + \delta T_{\text{perturbing.heat}} \tag{3.1}$$

where $\delta T_{\text{hydrostatic}} = 175\,\mu\text{K}$ is the hydrostatic pressure correction, $\delta T_{\text{isotopic}} = 70\,\mu\text{K}$ is the correction for isotopic composition of water, $\delta T_{\text{batch}} = 17\,\mu\text{K}$ is the correction for the difference from the average value of the French TPW national standard, and $\delta T_{\text{purity}} = \delta T_{\text{perturbing.heat}} = 0$ take into account corrections for water impurity and perturbing heat fluxes on the cell.

Three contact fluids were tested: Solvay Galden perfluorated oil 135, Castrol WOM 14 oil, and pure water. WOM 14 oil provided the shortest equilibration time for cooling the thermometer from room temperature to T_{TPW}. Changing the contact fluid in the well generated large changes in the self-heating of the thermometers; however, the resistance values corrected for self-heating were independent of the contact fluid.

Tests were also performed to evaluate the effect of the following parameters: change of resistance bridge, TPW cell stability, height of the contact fluid in the thermometric well, change in the contact fluid type, and changes in the wiring of the thermometers (particularly to evaluate the effect of the long wires installed in the thermostat). The uncertainty contributions associated to these parameters are summarized in Table 3, under the following names, respectively: $u(\delta r_{\text{bridge}})$, $u(\delta r_{\text{TPW.stability}})$, $u(\delta r_{\text{liquid.type}})$, $u(\delta r_{\text{liquid.level}})$, and $u(\delta r_{\text{cabling}})$. They are calculated as contributions to the ratio between the thermometer resistance and the resistance R_{S} of the standard resistor. Table 4 presents the complete uncertainty budgets for the calibrations at T_{TPW} of the four capsule-type thermometers. Details on the other uncertainty contributions are discussed in the following Sect. 3.1.2.

Table 3 Standard uncertainty components of CSPRT calibrations at the temperature of the triple point of water (T_{TPW}). (a) Components related to the TPW realization (purity, hydrostatic effect, …) and measurement conditions (cabling, liquid level in thermowell, …). (b) Uncertainties on the reference resistor R_S

Standard incertainity components of CSPRT calibrations at T_{TPW}					
Uncertainities related to TPW realization and measured conditions			Uncertainities on reference resistor R_s		
	$(10^7 \cdot \text{ratio})^a$	(mK^b)		$(\mu\Omega)$	(mK^b)
$u(\delta r_{bridge})$	0.51	0.01	$u(\delta R_{S,calibration})$	6.5	0.07
$u(\delta r_{TPW.stability})$	0.10	0.00	$u(\delta R_{S,time.drift})$	4.4	0.04
$u(\delta r_{cabling})$	1.23	0.03	$u(\delta R_{S,temperature.stability})$	1.4	0.01
$u(\delta r_{liquid.type})$	1.02	0.03			
$u(\delta r_{liquid.level})$	0.51	0.01			
$u(\delta r_{isotopic})$	0.41	0.01			
$u(\delta r_{hydrostatic})$	0.09	0.00			
$u(\delta r_{batch})$	0	0			
$u(\delta r_{purity})$	1.18	0.03			
$u(\delta r_{perturbing.heat})$	1.18	0.03			
Total (RSS)	**2.46**	**0.06**	**Total (RSS)**	**8.0**	**0.08**

[a] Uncertainties given for a nominal resistance ratio $R_{TPW}/R_S = 25.5\,\Omega/25\,\Omega$
[b] Equivalent uncertainties in temperature based on a nominal thermometer sensitivity $\partial R_{TPW}/\partial T = 0.1\,\Omega \cdot \text{K}^{-1}$

Table 4 Calibration of the thermometers at T_{TPW}

Calibration at T_{TPW} of the four thermometers installed on the acoustic resonator							
1551		**1825277**		**HS135**		**229073**	
Zero-current resistance at T_{TPW}							
25.580 871 5 Ω		**25.547 299 6 Ω**		**25.553 841 5 Ω**		**22.526 859 1 Ω**	
Uncertainty contributions of ratios and their equivalent in temperature							
$(10^7 \cdot \text{ratio})$	(mK)	$(10^7 \cdot \text{ratio})$	(mK)	$(10^7 \cdot \text{ratio})$	(mK)	$(10^7 \cdot \text{ratio})$	(mK)
3.54	0.09	6.04	0.15	5.8	0.14	10.38	0.29
4.31	0.11	6.52	0.16	6.3	0.15	10.61	0.3
Total combined standard uncertainty							
($u(\text{ratio})$ and $u(R_S)$ combined according to Eq. 3.5)							
Absolute standard uncertainty							
(mK)		**(mK)**		**(mK)**		**(mK)**	
0.14		**0.19**		**0.19**		**0.33**	
Relative standard uncertainty $\times 10^6$							
0.5		**0.7**		**0.7**		**1.2**	

Resistance values extrapolated to zero current and associated standard uncertainties

3.1.2 Results of Thermometer Calibration at T_{TPW}

Three series of calibrations at T_{TPW} were carried out on the four capsule-type ther-
mometers. The first was carried out in January 2009 prior to installing the resonator
BCU3 inside the thermostat for the first time, and hence prior to any acoustic mea-
surements using BCU3. The second and the third were carried out during September
and October 2009 after 7 months of acoustic experiments, during which the tempera-
ture was always close to T_{TPW}, but the thermometers were exposed to several pressure
cycles between near-vacuum and 0.7 MPa. Between the calibrations, the resistances of
three thermometers (1551, 1825277, HS135) at T_{TPW} changed less than the equivalent
of 0.15 mK. We considered them to be stable. In contrast, the thermometer 229073
exhibited changes larger than 0.3 mK that are inconsistent with the goal of these mea-
surements.

   For each thermometer, the resistance at the triple point of water was obtained via
the relation:

$$R_{TPW} = R_S \left(\overline{\overline{r}} + \delta r_{hydrostatic} + \delta r_{isotopic} + \delta r_{batch} + \delta r_{purity} + \delta r_{perturbing.heat} \right) \quad (3.2)$$

where R_S is the resistance of the standard resistor, $\delta r_{hydrostatic}$, $\delta r_{isotopic}$, δr_{batch}, δr_{purity},
and $\delta r_{perturbing.heat}$ are quantities proportional to the corrections $\delta T_{hydrostatic}$, $\delta T_{isotopic}$,
δT_{batch}, δT_{purity}, and $\delta T_{perturbing.heat}$ that we described above and are expressed as ratios
of the resistances of the thermometer to resistances of the reference resistor R_S.
   $\overline{\overline{r}}$ was calculated using the equations given in [27], Sect. 4.2:

$$\overline{\overline{r}} = \sum_{h=1}^{k} \sum_{i=1}^{n_h} r_{h,i} \bigg/ \sum_{h=1}^{k} n_h = \frac{1}{N} \sum_{h=1}^{k} (n_h \overline{r_h}) \quad (3.3)$$

Here k is the total number of calibration series, h identifies the calibration series
number, n_h is the number of measurements performed in the h-th series, $r_{h,i}$ is the
ith measurement in the h-th series, and corresponds to the ratio of the thermometer
resistance and the standard resistor resistance, extrapolated to zero current. $\overline{r_h}$ is the
average of the measurements in the h-th series and $N = \sum_{h=1}^{k} n_h$. In our case, $h = 3$
and $n_h \geq 3$; i.e., the measurements were repeated at least three times in each of the
three series. The variance associated to $\overline{\overline{r}}$ was calculated using

$$u \left(\overline{\overline{r}} \right)^2 = \frac{1}{N-1} \sum_{h=1}^{k} \sum_{i=1}^{n_h} \left(r_{h,i} - \overline{\overline{r}} \right)^2 \quad (3.4)$$

The overall standard uncertainty on the resistance at the triple point of water R_{TPW}
was calculated for each thermometer with the following relationship:

$$u (R_{TPW}) = \left((u \, (ratio) \, R_S)^2 + (u \, (R_S) \, R_{TPW}/R_S)^2 \right)^{1/2} \quad (3.5)$$

where u(ratio) is determined by the square root of the sum of squares (RSS) of the following terms: $u\left(\bar{r}\right)$, the uncertainty components $u(\delta r_{\text{bridge}})$, $u(\delta r_{\text{TPW.stability}})$, $u(\delta r_{\text{liquid.type}})$, $u(\delta r_{\text{liquid.level}})$, $u(\delta r_{\text{cabling}})$ previously mentioned, and the uncertainties associated to the quantities $\delta r_{\text{hydrostatic}}$, $\delta r_{\text{isotopic}}$, δr_{batch}, δr_{purity}, $\delta r_{\text{perturbing.heat,}}$ named, respectively, $u(\delta r_{\text{hydrostatic}})$, $u(\delta r_{\text{isotopic}})$, $u(\delta r_{\text{batch}})$, $u(\delta r_{\text{purity}})$, and $u(\delta r_{\text{perturbing.heat}})$. Values of these uncertainty components are provided in Table 3.

$u(R_{\text{S}})$ in Eq. 3.5 is determined by the RSS of the three uncertainty components $u(\delta R_{\text{S,calibration}})$, $u(\delta R_{\text{S,time.drift}})$, and $u(\delta R_{\text{S,temperature.stability}})$. These quantities, reported in Table 3, are uncertainties related, respectively, to R_{S} calibration, drift of R_{S} with time, and the temperature stability of the thermostat where the reference resistor is stored.

Table 4 provides the resistances R_{TPW} of the four thermometers at T_{TPW} extrapolated to zero current, as well as the list of the uncertainties contributing to u(ratio), and the final standard uncertainty budget, calculated for each of the four thermometers calibrated at T_{TPW}.

3.2 Temperature Measurements on the Acoustic Resonator

The four capsule-type thermometers calibrated at T_{TPW} were used to determine the average temperature of the resonator and to map the temperature distribution. Here, we describe the thermometer configurations that we used and the results that we obtained.

3.2.1 Experimental Configurations for Temperature Measurements

After the first calibration series (January 2009), thermometers 1551 and 1825277 were installed in the upper hemisphere, while 229073 and HS135 were installed in the lower one. This measurement configuration was named "C1" and corresponds to that represented in Fig. 9. Measurements were carried out for seven months in the C1 configuration. Then, the thermometers were dismounted, recalibrated at T_{TPW} (September and October 2009), and installed in a new configuration named "C2." This second configuration was used to perform measurements from February 2010 through September 2010.

The main differences between configurations C1 and C2 were the following:

- In C2, the positions of the thermometers 1551 and HS135 were swapped with respect to C1. The other thermometers were maintained in the same position.
- In C2, a pre-amplifier was installed and running on the bottom of the lower hemisphere. It dissipated approximately $70\,\mu\text{W}$, most of which was conducted away from the resonator by the argon in the pressure vessel and by the coaxial cable. To be certain, we conducted measurements to test for local heating of the resonator.
- Measurements in C1 and in C2 were carried out in argon. After the acoustic measurements in argon were completed, additional measurements were conducted in C2 in helium.

In both C1 and C2, the thermal drift of the resonator was minimized by controlling the temperature of the thermostat, particularly, the temperature of the thermal

shield. During the measurements, the temperature drifted less than $0.12\,\text{mK} \cdot \text{h}^{-1}$. We measured the drift with both acoustic and thermometric methods, and we found a strong correlation between the two measurements. This indicated that the temperature followed the same evolution in the shell of the resonator—where the temperature was measured with the CSPRTs—and in the gas inside, where the temperature was obtained by acoustic measurements. We concluded that the gas inside the resonator was thermalized at the same temperature of the shell, and that acoustic and CSPRT measurements gave the same temperature indication.

The four calibrated CSPRTs provided traceability to the temperature of the triple point of water. While they were installed in the resonator, we conducted self-heating measurements on them. The aim was to calculate the thermometer resistances at zero current to eliminate the effects of the thermal resistance between the thermometer sheaths and their housings. This was essential for making reliable comparisons of the resonator's temperature with the calibration data at T_{TPW} that were also extrapolated to zero current. Nevertheless, since the resonator's temperature drifted during self-heating measurements, a proper evaluation of the self-heating effect was difficult. Hence, we decided to determine such small temperature drifts with acoustic measurements and we applied a correction to the CSPRT measurements. The corrected CSPRT data appeared to be extremely flat within few tens of microkelvins, much like the temperature measurements conducted in exceptionally stable fixed-point cells. Figure 10 shows an example of data from the HS135 thermometer. The gray curve represents temperature data uncorrected from the thermal drift of the resonator, and the black curve shows the same data corrected from the thermal drift calculated from acoustic measurements. Using the corrected data, we obtained a reliable evaluation of the self-heating effect and we extrapolated the CSPRT measurements to zero current.

During the experiments, we carried out also tests for any possible change in the thermal homogeneity of the sphere due to a change in the temperature set point. The resonator was stabilized at various temperatures within the interval $T_{\text{TPW}} - 200\,\text{mK}$ to $T_{\text{TPW}} + 60\,\text{mK}$. For a similar reason, the gas pressure inside the pressure vessel was

Fig. 10 Temperature measurements carried out with a CSPRT. Measurements are realized with $1\,\text{mA}$ and $\sqrt{2}\,\text{mA}$ excitations, to evaluate the self-heating effect. *Gray points* represent raw measurements. *Black points* represent the same measurements corrected from the thermal drift of the resonator. The correction is evaluated from the acoustic measurement of the temperature
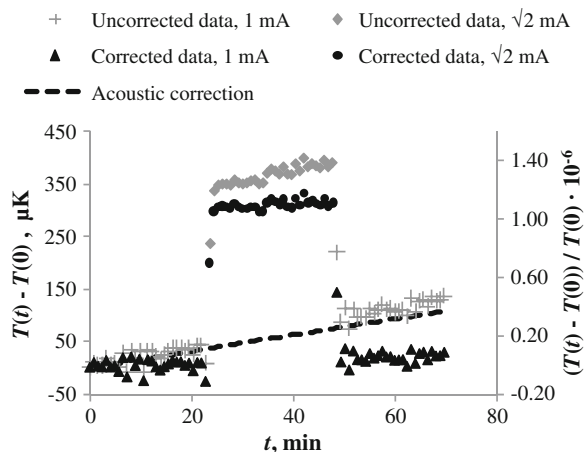
cycled several times between 0 MPa and 0.7 MPa and the temperature uniformity of the resonator was monitored. No changes in the thermal homogeneity of the resonator were observed with these tests.

Finally, the temperature of the external liquid bath was varied between −0.400 °C and −0.075 °C, to detect any possible correlation with the resonator's temperature. We did not observe any change in the temperature of the sphere. This proved that the resonator was thermally isolated from the liquid bath, and the temperature control of the thermal shield was able to compensate changes of several hundreds of a millikelvin in the temperature of the cold source.

3.2.2 Results of Thermal Mapping of the Resonator

Several thermal maps of the resonator were conducted in the configurations C1 and C2 previously described. For each thermal map, the resonator's average temperature was calculated as described below. First of all, for each thermometer, the difference ΔT between the temperature T_X of the acoustic resonator measured by the thermometer and T_{TPW} was expressed as:

$$\Delta T = T_X - T_{TPW} = S^{inv} (R_X - R_{TPW}) \tag{3.6a}$$

where S^{inv} is the inverse of the sensitivity of the thermometer (i.e., it is expressed in $K \cdot \Omega^{-1}$), R_X is the resistance of the thermometer at the temperature T_X, and R_{TPW} is the thermometer resistance at T_{TPW}. In our case, since we used the same reference resistor R_S for both the calibrations at T_{TPW} and the measurements on BCU3, it is possible to write

$$\Delta T = S^{inv} (R_X - R_{TPW}) = S^{inv} R_S (r_X - r_{TPW}) \tag{3.6b}$$

where $r_X = R_X/R_S$ and $r_{TPW} = R_{TPW}/R_S$.

Then, the standard combined uncertainty on ΔT was calculated using

$$u(\Delta T) = \sqrt{(R_S (r_X - r_{TPW}))^2 u^2 (S^{inv}) + (S^{inv} (r_X - r_{TPW}))^2 u^2 (R_S)}$$
$$\sqrt{+ (S^{inv} R_S)^2 (u^2 (r_X) + u^2 (r_{TPW}))} \tag{3.7}$$

Finally, the average temperature of the resonator $\overline{\Delta T}$ was calculated as the mean of the ΔT terms calculated for each of the three thermometers, 1551, 1825277, and HS135. Thermometer 229073 was not included in the calculations, because it was unstable at T_{TPW}. The reader should note that $\overline{\Delta T}$ expresses the average temperature of the resonator with respect to the temperature of the triple point of water, and not in an absolute way, because it is obtained from the relative terms ΔT.

An estimate of the uncertainty on $\overline{\Delta T}$ was calculated according to the equation (4.3.6) in [27]:

$$u\left(\overline{\Delta T}\right) = \frac{(\max\{\Delta T_{1551}, \Delta T_{1825277}, \Delta T_{HS135}\} - \min\{\Delta T_{1551}, \Delta T_{1825277}, \Delta T_{HS135}\})}{2}$$

(3.8)

Table 5 summarizes the results of nine different thermal maps, labelled Tm1 to Tm9, carried out on BCU3. Four of them were conducted in the configuration C1 in argon, at four different temperatures, and four in the configuration C2, in argon, also at four different temperatures. The ninth map was also conducted in the configuration C2, but using helium instead of argon.

The results presented in Table 5 are drawn also in Fig. 11, where the values $\Delta T - \overline{\Delta T}$ are plotted, and the associated standard uncertainty bars correspond to the values $u(\overline{\Delta T})$.

Figure 11 shows the nine thermal maps of the resonator, Tm1 to Tm9. In each thermal map the average temperature $\overline{\Delta T}$ of the resonator is changed, from $-223.07\,\mathrm{mK}$ below the temperature of the triple point of water to $69.86\,\mathrm{mK}$ above T_{TPW}. We can observe that no thermal gradients appear on the resonator's shell at any $\overline{\Delta T}$, provided that the quasi-sphere is maintained at a temperature within few tens of millikelvins of T_{TPW}.

Looking at Fig. 11 and the numerical results of Table 5, and in particular at the values $u\left(\overline{\Delta T}\right)$, it is possible to have a clear idea of the order of magnitude of the standard uncertainty that can be associated to any thermal map conducted on the resonator. This value is below 0.1 mK, and formal calculations will be provided in the following Sect. 3.3.

3.3 Final Uncertainty Budget on Temperature Measurements

The values $u\left(\overline{\Delta T}\right)$ shown in Table 5 provide an indication of the uncertainty for a single thermal map, but an overall estimate of the uncertainty in temperature measurements has to be determined, to be assigned to the determination of the Boltzmann constant with BCU3. As shown in Sect. 3.2.2, the thermal maps provide the resonator's average temperature $\overline{\Delta T}$, and we use this average to scale acoustic measurements to T_{TPW}. For each thermometer, the deviation $\Delta T - \overline{\Delta T}$ expresses the deviation of the thermometer from the average temperature $\overline{\Delta T}$, or equivalently the deviation from T_{TPW} when the resonator's temperature is scaled to T_{TPW}.

Because all the deviations $\Delta T - \overline{\Delta T}$ shown in Table 5 can be considered as related to T_{TPW}, it is possible to calculate a general mean and a general standard deviation on the values of $\Delta T - \overline{\Delta T}$ using Eqs. 3.3 and 3.4.

We introduce the notation, $\Delta T_{h,i}^{\mathrm{TPW}}$ for the i-th deviation $\Delta T - \overline{\Delta T}$ of the h-th thermal map, i.e., $\Delta T_{h,i}^{\mathrm{TPW}} \equiv \left(\Delta T - \overline{\Delta T}\right)_{h,i}$ and we define

Table 5 Results of nine different thermal maps of BCU3

N.th.	r_X	$10^5 \cdot u(S^{inv})$ $(K \cdot \Omega^{-1})$	ΔT (mK)	$\overline{\Delta T}$ (mK)	$\Delta T - \overline{\Delta T}$ (mK)	$u\left(\overline{\Delta T}\right)$ (mK)
		Tm1: C1, Ar, $\overline{\Delta T} = 7.21$ mK				
1551[a]	1.023 263 97(15)	0.5	7.30(11)	**7.21**	0.09	**0.10**
1825277[b]	1.021 920 79(10)	0.3	7.23(16)		0.02	
HS135[c]	1.022 181 91(10)	0.4	7.09(16)		−0.11	
		Tm2: C1, Ar, $\overline{\Delta T} = 6.59$ mK				
1551	1.023 261 15(12)	0.3	6.60(11)	**6.59**	0.02	**0.10**
1825277	1.021 918 54(13)	0.5	6.68(16)		0.09	
HS135	1.022 179 41(14)	0.6	6.48(16)		−0.11	
		Tm3: C1, Ar, $\overline{\Delta T} = 8.66$ mK				
1551	1.023 269 70(10)	0.9	8.70(11)	**8.66**	0.04	**0.07**
1825277	1.021 926 81(10)	0.1	8.71(16)		0.05	
HS135	1.022 187 92(12)	0.0	8.57(16)		−0.09	
		Tm4: C1, Ar, $\overline{\Delta T} = -15.86$ mK				
1551	1.023 170 38(17)	6.4	−15.64(11)	**−15.68**	0.04	**0.07**
1825277	1.021 827 62(09)	7.2	−15.63(16)		0.05	
HS135	1.022 088 68(06)	7.2	−15.77(16)		−0.09	
		Tm5: C2, Ar, $\overline{\Delta T} = 65.21$ mK				
1551	1.023 500 33(09)	18.5	65.21(11)	**65.21**	0.00	**0.05**
1825277	1.022 157 30(11)	17.8	65.26(16)		0.05	
HS135	1.022 418 65(22)	18.0	65.16(16)		−0.05	
		Tm6: C2, Ar, $\overline{\Delta T} = 69.86$ mK				
1551	1.023 519 36(05)	20.0	69.87(11)	**69.86**	0.02	**0.07**
1825277	1.022 176 30(11)	19.2	69.92(16)		0.06	
HS135	1.022 437 45(11)	19.4	69.77(16)		−0.08	
		Tm7: C2, Ar, $\overline{\Delta T} = 8.00$ mK				
1551	1.023 267 04(17)	1.4	8.05(11)	**8.00**	0.04	**0.06**
1825277	1.021 924 08(20)	0.6	8.04(17)		0.03	
HS135	1.022 185 33(27)	0.8	7.93(17)		−0.07	
		Tm8: C2, Ar, $\overline{\Delta T} = 8.66$ mK				
1551	1.023 269 68(15)	1.6	8.69(11)	**8.66**	0.03	**0.06**
1825277	1.021 926 79(10)	0.8	8.70(16)		0.04	
HS135	1.022 188 01(13)	1.0	8.59(16)		−0.07	
		Tm9: C2, He, $\overline{\Delta T} = -223.07$ mK				
1551	1.022 323 92(04)	68.2	−223.03(11)	**−223.07**	0.05	**0.12**
1825277	1.020 982 43(04)	68.5	−222.98(16)		0.09	
HS135	1.021 242 92(11)	68.8	−223.21(16)		−0.14	

$R_S = 25.000\ 016\ 2\ \Omega$, $u(R_S) = 6.5\ \mu\Omega$

[a] Thermometer 1551: $r_{TPW} = 1.023\ 234\ 2(04)$; $S^{inv} = 9.801\ 1\ K \cdot \Omega^{-1}$

[b] Thermometer 1825277: $r_{TPW} = 1.021\ 891\ 3(07)$; $S^{inv} = 9.813\ 9\ K \cdot \Omega^{-1}$

[c] Thermometer HS135: $r_{TPW} = 1.022\ 153\ 0(06)$; $S^{inv} = 9.811\ 4\ K \cdot \Omega^{-1}$
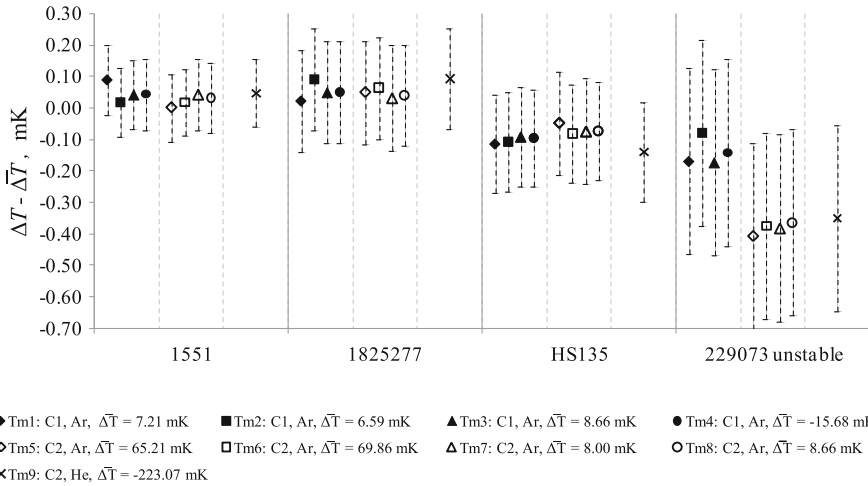
◆ Tm1: C1, Ar, $\overline{\Delta T}$ = 7.21 mK   ■ Tm2: C1, Ar, $\overline{\Delta T}$ = 6.59 mK   ▲ Tm3: C1, Ar, $\overline{\Delta T}$ = 8.66 mK   ● Tm4: C1, Ar, $\overline{\Delta T}$ = -15.68 mK

◇ Tm5: C2, Ar, $\overline{\Delta T}$ = 65.21 mK   ▢ Tm6: C2, Ar, $\overline{\Delta T}$ = 69.86 mK   △ Tm7: C2, Ar, $\overline{\Delta T}$ = 8.00 mK   ○ Tm8: C2, Ar, $\overline{\Delta T}$ = 8.66 mK

✕ Tm9: C2, He, $\overline{\Delta T}$ = -223.07 mK

Fig. 11 Plot of $\Delta T - \overline{\Delta T}$ values and the associated standard uncertainty bars $u(\Delta T)$ for the four thermometers. Nine thermal maps of the resonator are shown (Tm1 to Tm9). Measurements are carried out in configuration C1 or C2, with either argon (Ar) or helium (He), at different resonator's average temperatures $\overline{\Delta T}$

$$\overline{\overline{\Delta T^{\mathrm{TPW}}}} \equiv \sum_{h=1}^{l} \sum_{i=1}^{m_h} \Delta T_{h,i}^{\mathrm{TPW}} \bigg/ \sum_{h=1}^{l} m_h \qquad (3.9)$$

and the associated variance,

$$u\left(\overline{\overline{\Delta T^{\mathrm{TPW}}}}\right)^2 = \frac{1}{M-1} \sum_{h=1}^{l} \sum_{i=1}^{m_h} \left(\Delta T_{h,i}^{\mathrm{TPW}} - \overline{\overline{\Delta T^{\mathrm{TPW}}}}\right)^2 \qquad (3.10)$$

where m_h is the number of thermometers measured in the h-th thermal map ($m_h = 3$ in all our thermal maps), l is the total number of thermal maps realized ($l = 9$ in our case), and $M = \sum_{h=1}^{l} m_h$.

From the definition of $\Delta T_{h,i}^{\mathrm{TPW}}$, it can be shown that $\sum_{i=1}^{m_h} \Delta T_{h,i}^{\mathrm{TPW}} = 0$ for each thermal map, and hence $\overline{\overline{\Delta T^{\mathrm{TPW}}}} = 0$, which means that the overall mean has zero deviation from T_{TPW}. Then, we use the standard deviation $u\left(\overline{\overline{\Delta T^{\mathrm{TPW}}}}\right)$ to estimate the standard uncertainty of temperature measurements on BCU3 in argon. By applying Eq. 3.10 to the values given in Table 5, we obtain the standard uncertainty of the

Table 6 Standard uncertainty on temperature measurements on BCU3 in argon

Overall Standard uncertainty on temperature measurement	
$u_{\mathrm{temperature}}$	$0.07\,\mathrm{mK}$
$\dfrac{u_{\mathrm{temperature}}/\mathrm{K}}{273.16/\mathrm{K}}$	0.3×10^{-6}

temperature of 0.07 mK which corresponds to a standard relative uncertainty of 0.3 parts in 10^6 at T_{TPW}. Table 6 summarizes these results.

4 Measurement of the Volume of the Resonator

This section describes how the equivalent radius a_{eq} of the quasi-spherical resonator (QSR) was estimated and how its standard uncertainty $u(a_{eq})$ was calculated. The equivalent radius is used to determine the volume of the QSR, and is one of the elements used for the determination of the Boltzmann constant. We determined a_{eq} from measurements of the resonance frequencies of microwave modes and calculations of their eigenvalues, as mentioned in Sect. 1.

In 1986, Mehl and Moldover [12] used first-order perturbation theory to prove that the mean eigenfrequency of a multiplet is independent of volume-preserving deformations, and suggested that the volume of an imperfect spherical resonator could thus be determined from its microwave spectrum. Several of our earlier papers have set the groundwork for this determination [2,3,16,20,22].

We determined the average radius of BCU3 by measuring the frequencies and half-widths of nine microwave triplets and correcting the measurements for three effects:

– the microwave penetration depth using measured half-widths of the resonances, as described in [2];
– the inlet and outlet gas ducts and the two microwave antennas using the extensive study of the effects of probes and holes in a QSR performed by Underwood et al. [22];
– the shape of the QSR, using Mehl's second-order theory [21] and our measurements of the frequency splitting of the microwave triplets.

Our determination of the equivalent radius and its uncertainty budget was accomplished in four steps:

1. At 20 °C and using straight microwave antennas (probes), we measured the frequencies of 5 TM microwave triplets while the microphone ports were closed with blank copper plugs (see Sect. 2.1.3). We corrected these frequencies to account for shape and probe perturbations using the models and the results in [22].
2. With loop antennas, we determined the electrical conductivity of the copper surface and established a bound on any dielectric layer on the surface, in the same experimental conditions (20 °C and flowing argon) as those specified for step 1.
3. After having replaced the blank ports, we obtained the final equivalent radius of the QSR with the acoustic microphones and loop antennas installed on it.
4. We estimated the resonator's compressibility on isotherms, and we measured the resonator's thermal contraction upon cooling from 20 °C to T_{TPW}. The thermal expansion coefficient and the compressibility of the resonator are used to calculate the very small corrections needed to account for the change of the resonator radius as a function of temperature and pressure.

4.1 Volume of the Resonator with Straight Probe Antennas

First, we determined the volume of BCU3 at 20 °C using straight probe antennas. The microwave measurements were made using an Agilent E5071C ENA network analyzer locked to a SRS rubidium clock (SRS SIM940). (The same clock was used for the acoustic measurements). The analyzer measured the complex voltage scattering parameter S_{12} using frequency sweeps of 200 points spanning each of the microwave triplets designated TM11, TM12, TM13, TM14, and TM15. The data from the analyzer were fitted by a complex resonance function, described in [20].

During these measurements at 20 °C, 1 m coaxial cables connected the network analyzer to the resonator to minimize the attenuation of the microwave signals. Two small, coaxial antennas were mounted in the quasi-sphere such that their central conductors were flush with the inner surface of the cavity. Note: During normal operation, BCU3 was installed in its thermostat where 3 m long coaxial cables, 2.3 mm outer diameter, silver-plated, connected the microwave antennas to feedthroughs on the top of the thermostat. These long cables were necessary for reducing heat conduction to the resonator. The cables attenuated the microwave signals; however, they did not affect the frequency and half-width measurements. In the configuration with the three-meter coaxial cable, the microwave power heated the sphere by no more than 0.75 mK. The extrapolation of the frequency measurements to zero power did not change the resonance frequency values, and the determinations of a_{eq} were in agreement within the standard deviation of ± 3.2 nm. During the 20 °C measurements, the ports for the acoustic transducers were closed with copper plugs that had been machined in place at the same time that the inner surface of the cavity was diamond-turned. Thus, the surfaces of the plugs closely matched the surrounding quasi-spherical surface. In addition to the microwave ports, two small ducts carried gas inside and outside the sphere. Argon gas was flowed through the sphere and its temperature and pressure were measured. In this way the results were corrected for changes in the refractive index of argon as a function of density [28].

The radius of the sphere was obtained by measuring the microwave modes from TM11 to TM15 and correcting the data by the second-order shape effect and the probe effect. The amplitude of the probe correction was 134.3 nm for the TM11x and TM11y, and 89.5 nm for the TM11z. The second-order shape correction for the TM11 was 6.8 nm. The results for the five TM1n modes were mutually consistent within a standard deviation of ± 8.6 nm (Fig. 12). This demonstrated the self-consistency of both the second-order shape correction and the probe correction. The flow of argon gas allowed us to have very reproducible results over a period of three months, even while the thermostat was not operating and the QSR was at room temperature. (During this period, the QSR temperature was measured and corrections were applied to account for temperature variations).

We conducted an additional experiment to test the reliability of the microwave measurements of the QSR radius. We installed a third antenna at the microphone port 2 (see Fig. 5) and determined new values for the radius using three different combinations of transmitting and receiver antennas. No changes were observed at the level of 0.08 parts in 10^6, which was our noise limit at that time, with or without a cable connected to the unused antenna. Remarkably, after correcting for the presence of the third antenna and
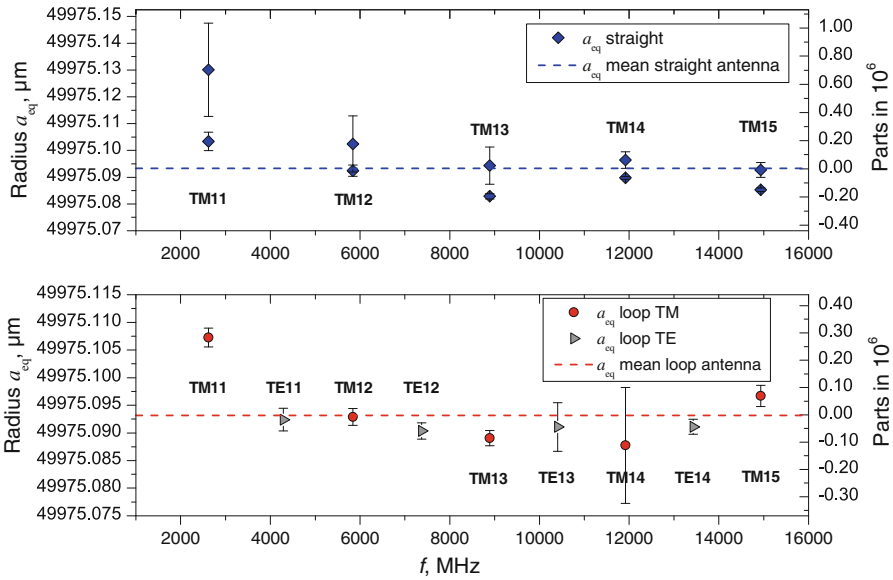
Fig. 12 Radius measured with the straight antennas and with the loop antennas. Three months is the time between the two different series of data taken for the straight antennas
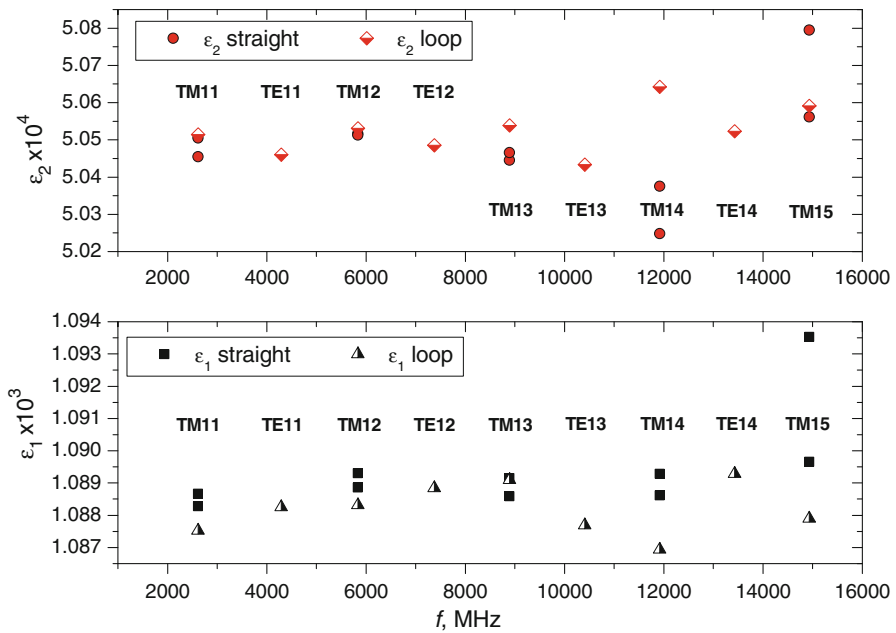

Fig. 13 Shape parameter of the QSR measured with straight antennas and with loop antennas

its port using [22], the difference $(a_{\mathrm{eq,3antennas}}) - (a_{\mathrm{eq,2antennas}}) = 0.17(11) \times 10^{-6}$, which corresponds to a length difference of 8.6 nm.

The microwave frequency measurements enabled us to confirm that the two hemispheres forming BCU3 were nearly perfectly aligned. In a perfect quasi-sphere, the amplitudes of the modes TM11x, TM11y, and TM11z should be in the ratios 1:1:2 [29]. (Here, TM11x refers to the component of the TM11 symmetric about the x axis, etc.) In our case (see Fig. 7) and in first approximation the ratios were 1:1.05:1.86. In contrast, the ratios were 1:1.25:1.82 in Fig. 6 from [25]. In [25], the amplitude ratio TM11y:TM11x = 1.25 corresponded to a misalignment of 6 μm. In our case, the ratio TM11y:TM11x = 1.05 corresponds to a misalignment of approximately 1 μm.

4.2 Volume of the Resonator with Loop Antennas

4.2.1 Volume Determination with Loop Antennas and Without Microphones

We performed microwave measurements with loop antennas for the following reasons:
– Because the loops couple to TE modes (as well as TM modes), we can obtain additional information about a_{eq}.
– The signals generated by our loops were approximately 20 times stronger than the signals generated by our straight probes.
– A comparison of the results from the TM modes with the results from the TE modes can provide information about the surface of the cavity (such as the presence of a dielectric layer) because the TE modes are much less sensitive to the surface perturbations than the TM modes.
– We estimated the electrical conductivity of our copper resonator at microwave frequencies from measurements of the half-width of the TE11z mode and Eqs. (6) and (7) in [20]. The electrical conductivity is needed to calculate the distance that the microwaves penetrate into the copper, i.e., the skin depth. The TEz modes are the best modes for this purpose, because electrical currents flow around the z axis; therefore, they are not perturbed by the seam where the two hemispheres meet [30].

The downside of using loop antennas is that there are no models to accurately calculate the frequency perturbations generated by the loop. As described in [22], the perturbations to the TM frequencies are small (around 1 part in 10^6). Therefore, we decided to estimate the perturbations by using a substitution method.

We assumed that the volume of the quasi-sphere was the same whether it was measured with straight or loop antennas. Following the advice of Underwood[2], we set the coefficient for the term $\varepsilon_0|E_{n,b}|^2$ in Eq. (23) of [22] tend to zero to take into account the increased relative permittivity of the cylindrical volume around the waveguide. This choice primarily affects the equivalent radius $a_{\mathrm{eq,TM11}}$ determined using the mode TM11.

We installed the loop antennas in the same ports that we had used for the straight antennas, and we left the copper plugs in the microphone ports undisturbed.

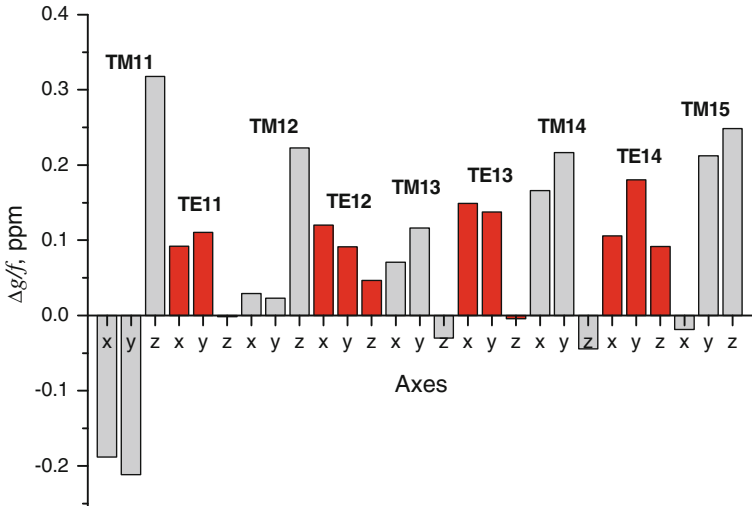[2] Private communication from Robin Underwood, NPL.

Fig. 14 Excesses of half-width determined using the electrical conductivity obtained with the mode TE11z

As the graphs in Fig. 12 show, the a_{eq} radii obtained for several TM and TE modes with the straight and loop antennas are in very good agreement (standard deviation of 4.5 nm). The values of the two parameters of ε_1 and ε_2 determined with the two types of antennas show differences within 0.2 %.

From the half-width of the TE11z mode, we obtained an electrical conductivity of 1.61×10^{-8} $\Omega \cdot$ m at 0.01 °C. Using this value, we computed the half-widths of the other modes. In Fig. 14, we compare the measured and computed half-widths scaled by the frequency. The half-width of the TE11 was on average lower by 0.08 parts in 10^6. A standard deviation of 0.09 parts in 10^6 is obtained from the excesses of half-width with the conductivity obtained with the mode TE11z as a reference. This value is the estimate of our uncertainty on the copper electrical conductivity.

These results gave us the confidence to use loop antennas instead of the straight ones. We gained a stronger signal, a reduced sensitivity to surface perturbations, and a measurement of the electrical conductivity of the copper. We gave up the mathematical model for the straight antennas. The differences between the radius values a_{eq} obtained with loop antennas and those obtained with straight antennas quantify this loss. The difference $(a_{eq,loop}) - (a_{eq,straight}) = 5.8(8.5)$ nm, which corresponds to a relative uncertainty $u_r(a_{eq}) = 5.4 \times 10^{-8}$. At this level, loop antennas and straight antennas provide equivalent results.

4.2.2 Volume Determination with Loop Probe Antennas and with Microphones

After the determination of the QSR volume with loop antennas and without microphones, we installed two 1/4 inch (6.35 mm) diameter microphones in the resonator. The blank plugs were removed and the acoustic transducers fitted in.

The equivalent radius obtained from microwave measurements after the two microphones were installed, was 23 nm bigger than the measured equivalent radius without

Table 7 Typical equivalent radii obtained at 0.1 MPa and at 273.16 K with loop antennas and microphones

Mode	Frequency (MHz)	Equivalent radius (μm)	Equivalent radius deviation [a] (ppm)	Uncertainty of equivalent radius (μm)	ε_1	ε_2
TM11	2 619.332 654	49 958.484 5	0.13	0.002 3	0.001 077	0.000 506
TM12	5 839.489 169	49 958.479 39	0.02	0.002 2	0.001 079	0.000 506
TM13	8 894.290 939	49 958.475 88	−0.05	0.006 6	0.001 079	0.000 506
TM14	11 919.946 23	49 958.476 75	−0.03	0.005 1	0.001 078	0.000 507
TM15	14 934.746 37	49 958.475 79	−0.05	0.008 0	0.001 077	0.000 505
TE11	4 289.721 942	49 958.476 6	−0.03	0.002 7	0.001 078	0.000 506
TE12	7 375.063 569	49 958.479 41	0.02	0.004 5	0.001 078	0.000 506
TE13	10 409.834 7	49 958.476 75	−0.03	0.007 4	0.001 079	0.000 505
TE14	13 428.568 8	49 958.478 61	0.01	0.004 7	0.001 080	0.000 506

[a] Deviations calculated with respect to the average of the equivalent radius values

microphones. The radius difference was due to the slightly imperfect positioning of the microphone cartridges with respect to the internal surface of the sphere. This was true for both the TE and TM modes (see Table 7) and over a factor of 5.7 in frequency, and the scatter among the modes was again extremely small. With the microphones inserted, the values of ε_1 and ε_2 determined using the only TM modes were equal to those determined using the only TE modes, and the two respective radius determinations were equal within 0.05 parts in 10^6. We cannot think of any phenomenon that might generate the same fractional perturbation to the frequencies of all five TM modes and all four TE modes. (Such a phenomenon would generate an undetectable bias in all the values of a_{eq}). We conclude that the insertion of the microphones did not modify the inner QSR volume in a significant way. In [31], the authors have obtain the same conclusion.

To corroborate our thesis and to estimate the uncertainty component related to the microphone insertion, we now consider another experiment that demonstrated that the changes in the volume measured by microwave resonances are proportional to the changes in the volume of the QSR when the perturbations on the wall are small.

A preliminary version of the experiment was conducted in collaboration with NPL to understand the effect of a hole in a QSR [22]. As shown in Fig. 15, a cylinder fitting snugly in a 2.3 mm diameter hole was inserted into the cavity at a distance h_C measured from the surface of the cavity. The frequencies of each component of the triplet TM11 were measured as a function of the displacement. The average frequency of the triplet followed the change of the volume for displacements of several tenths of a millimeter. For larger displacements, the average frequency perturbation is a more complicated function of h_C, but can be analyzed [29]. In the range where the average frequency follows the change in volume, the difference between the actual volume and the volume determined from the TM11 mode is less than 0.1 parts in 10^6. For the other modes, such as the TM12, the range in which the average frequency follows the volume perturbation is smaller.

Figure 15 suggests the method that we used to estimate the uncertainty due to the microphone insertion: because the mode TM11 follows the volume change over a
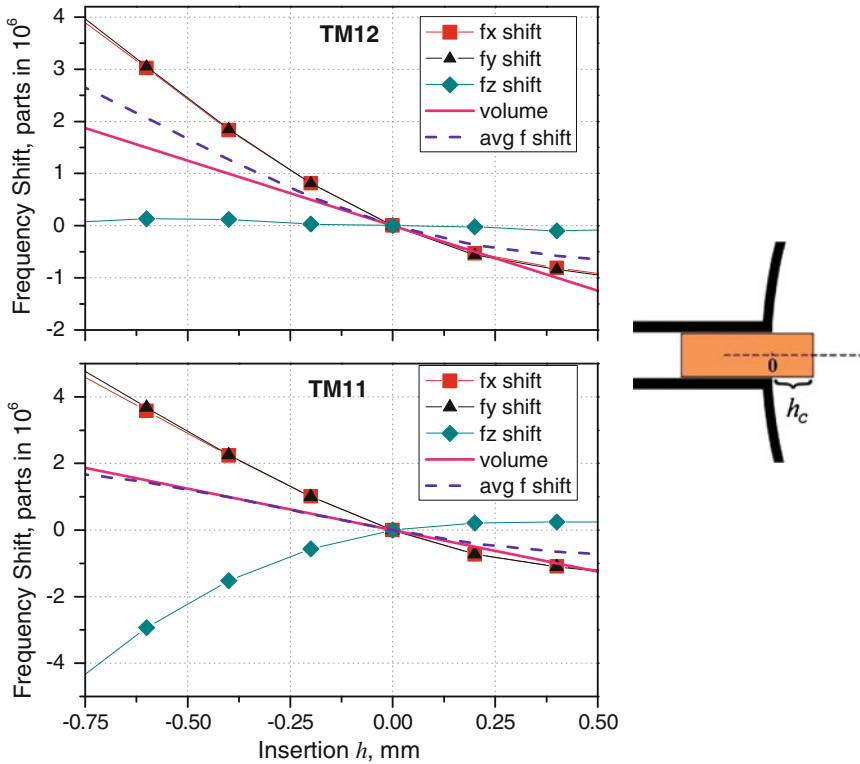
Fig. 15 Change in volume caused by a small cylinder entering the sphere, as detected by the TM11 and TM12 modes

much larger insertion distance than the other modes, the difference between the radius estimated by the mode TM11 and the radii estimated by the other TM modes is the estimator of the uncertainty component related to the insertion of the microphone.

Table 7 shows the typical equivalent radii obtained at 0.1 MPa and at 273.16 K with loop antennas and microphones.

The use of the loop antennas can also give a very precise estimate of the presence of a layer of impurities on the surface as demonstrated in [20]. The difference between the average radius estimated using only TE modes and that estimated using only TM modes provides an estimation of the presence of such a layer. According to [25], we estimated a 10 nm copper oxide layer because $a_{\text{eq.TM11}} - \langle a_{\text{eq.TE}} \rangle = 3.4$ nm, where $a_{\text{eq.TM11}}$ is the equivalent radius calculated with the TM11 mode and $\langle a_{\text{eq.TE}} \rangle$ is the average of the radii calculated with the TE modes.

4.3 Compressibility and Thermal Expansion of the Resonator

All the measurements were carried out using the modes TM11 to TM15 and TE11 to TE14, because of the losses in the microwave feedthroughs and cables.

The temperature dependence of the equivalent radius $a_{eq}(T)$ was deduced from measurements of the frequencies of the TE and TM modes at constant pressure during controlled warming of the resonator [2]. The coefficient of linear expansion of the resonator $\alpha = (da_{eq}/a_{eq})/dT$ [1] was $16.39 \times 10^{-6} \text{m} \cdot \text{m}^{-1} \cdot \text{K}^{-1}$ at $0\,^\circ\text{C}$, with an uncertainty of 0.03×10^{-6}.

The pressure dependence of the radius was measured from $0.05\,\text{MPa}$ to $0.7\,\text{MPa}$ at the temperature $0.01\,^\circ\text{C}$. The radius at the highest pressure was, fractionally, 0.3×10^{-6} smaller than the radius at the lowest pressure. The main uncertainty of this measurement comes from the uncertain pressure dependence of the refractive index of argon [28].

Two isotherms were realized, and the compressibility was found to be 22 % and 30 % larger than the value reported by May et al. [20]. However, our results were consistent with those of May et al. [20], within the uncertainty of our measurement. The values of ε_1 and ε_2 were independent of the pressure.

The value and the uncertainty of k_B are independent of the compressibility, because the resonance frequency variation due to the compressibility change is a linear function of the pressure, and the evaluation at zero pressure given by $\lim\limits_{p \to 0}^{*} \left(c_a^2(p, T_{TPW}) \right)$ in Eq. 1.1 eliminates this dependence.

4.4 Uncertainty Budget Associated to the Equivalent Radius Measurement

Table 8 summarizes the budget of the uncertainties associated to the determination of the equivalent radius of the resonator, and hence those associated to the volume determination.

Table 8 Uncertainty budget associated to resonator's radius determination for determining the Boltzmann constant

Uncertainty component	Effect on k_B in parts in 10^6	Note
Resonance fit	0.087	Fit uncertainty
Scatter among microwave radii (includes uncertainty of shape perturbation)	0.32	Agreement between the TE and TM modes
Frequency reference	0.0	<1 part in 10^{10}
Temperature calibration	0.009	As described in Sect. 3 temperature
Temperature gradient	0.009	As describe in Sect. 3, temperature gradient less than 0.1 mK
Surface conductivity	0.22	Scatter of the average conductivity relative to the conductivity obtained using the TE11z mode
Microphone perturbation	0.37	Difference between the radius obtained with the TM11 mode and that of the other modes
Waveguide corrections	0.15	Difference between the radii observed with straight antennas and with loop antennas
Dielectric layer	0.06	Difference in the radii obtained with only TM modes and only TE modes
Total	0.57	Square root of the sum of squares

In 1988, Mehl and Moldover [12] suggested that the volume of an imperfect spherical resonator could be determined from its microwave spectrum, although they could not achieve accurate measurements at that time. Today, we are confident that the substitution measurements validated our corrections with fractional uncertainties well below 10^{-6} for the ducts and for the loop antennas.

5 Measurements and Analysis of the Acoustic Data

For the acoustic measurements, the experimental techniques and data analysis methods are built on foundations established over two decades by Moldover et al. [1,11] and subsequently applied to temperature measurements from 7 K to 552 K [16,32,33].

5.1 Description of the Acoustic Measurement Method and of the Data Processing Procedure

5.1.1 Apparatus and Equipment

The experimental apparatus allows the measurement of the radial acoustic modes from (0,2) through (0,5), and also (0,8) and (0,9), at several pressures between 0.05 MPa and 0.7 MPa. During our experiments with BCU3 filled with argon, these measurements were repeated at least 15 times under these conditions.

Two 1/4 inch (6.35 mm) B&K 4939 microphones were used, one acting as the acoustic source and the other as the receiver. They were mounted to be flush with the inner surface, to minimize perturbations on the measurement of the QSR volume, as described in Sect. 4. The source was directly driven from a frequency-synthesized sine wave generator (SRS DS335) locked to a rubidium clock (SRS SIM940). The source transducer was polarized at 130 V and driven by a 60 V peak-to-peak signal generated by a Krohn-Hite 7602M wide band amplifier. These parameters were chosen to efficiently drive the source transducer, and depend on the parasitic capacitances of our system. We studied the effect of changing the voltage driving the acoustic source transducer, in a QSR very similar to BCU3 (same dimensions, same material, and analogous thermostat) [3]. The temperature of the resonator, the pressure inside, the gas flow rate, and the polarization voltage on the source transducer were maintained constants and no effect was observed [3]. We measured also the changes in half-widths when the amplitude of the driving voltage was changed from 15 V to 60 V peak-to-peak in argon at 0.1 MPa, and we found that they were less than 0.15 parts in 10^6.

The receiver microphone was polarized at 130 V and its signal was conditioned in three different ways. In the first configuration, the signal was carried from the resonator through a 4 m long coaxial cable to the vacuum feedthrough, and then from the feedthrough to a lock in amplifier (SRS 830) used in its current mode. In the second configuration, we inserted an amplifier between the outer side of the feedthrough and the coaxial cable leading to the lock-in amplifier. The amplifier was a type 26AC preamplifier from GRAS connected to a GRAS Type 12AA power module and is labelled "Optional Amplifier" in Fig. 16.
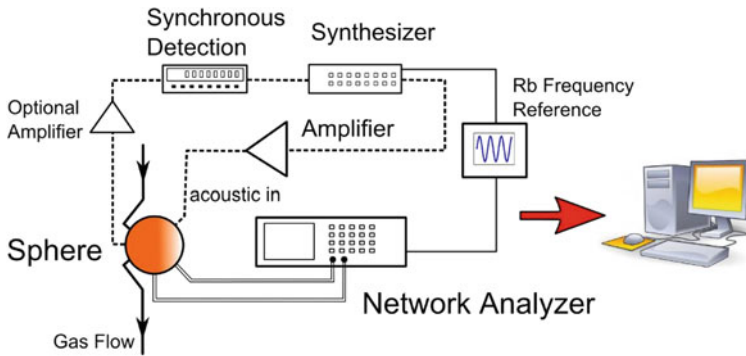
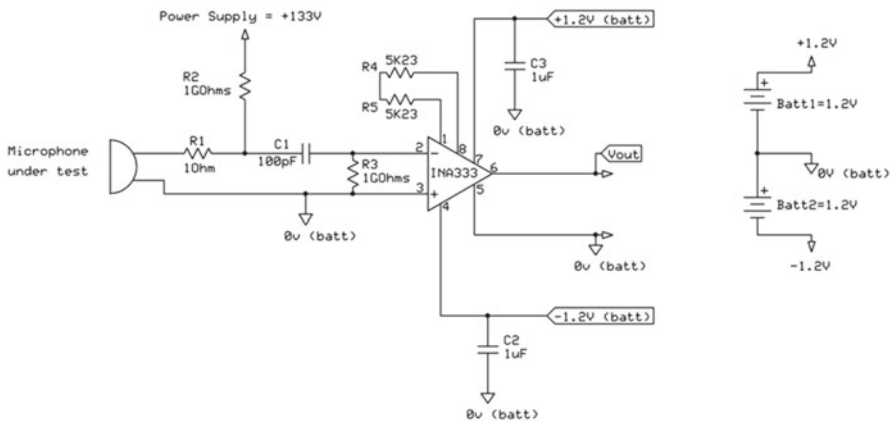**Fig. 16** Schematic diagram of the acoustic and electromagnetic acquisition systems

Fig. 17 Schematic of the preamplifier plugged very close to the microphone. The heating power was configured to be below 70 μW. The two commercial batteries powered the circuit for more than 15 months

The third configuration was set-up after the argon measurements were completed and was used for additional isotherm measurements performed with helium gas. In this third configuration a home-made preamplifier was installed very close to the receiver microphone: the signal was then carried through the 4 m long coaxial cable up to the feedthrough, and then to the lock-in amplifier outside the thermostat. An electronic schematic of the home-made preamplifier is given in Fig. 17. With this last configuration, we estimated the acoustic pressure field inside the cavity from the sensitivity of the microphone. We found that it was a few pascals at 4.4 kHz and less than 1 Pa at 27 kHz. We concluded that the sound pressure is negligible compared with any of the static operating pressures between 0.05 MPa and 0.7 MPa.

All three configurations provided the same signal-to-noise ratio, and hence were considered equivalent.

During isotherm measurements, gas flowed through the resonator. The impedance of the inlet and outlet tubes created a pressure difference between the upstream and downstream parts of the gas manifold. The upstream and downstream pressures were

measured by two Digiquartz® 745 manometers (0.7 MPa maximum pressure). Because the lengths and radii of the tubes were very well known, we were able to estimate the pressure in any point of the gas handling system, and therefore in the QSR. At all the pressures, we were able to estimate the gas flow rate in the tubing, and these values agreed with independent measurements made with a flow meter AERA7800. From the impedances of the tubes and the Hagen–Poiseuille equation, we estimated that the pressure in the resonator was $0.9663\,p_{outlet} + 0.0337\,p_{inlet}$. One year after the initial calibrations, the manometer calibrations were checked at one pressure and they were still within the manufacturer's specifications.

Following the procedures described above and using the apparatus shown in Fig. 16, two argon isotherms at T_{TPW} were measured: the first one in May 2009, and the second one in July 2009. The first isotherm lasted 2 weeks during which measurements at 13 different pressures were realized. In the second isotherm, measurements at a total of 26 different pressures between 0.05 MPa and 0.7 MPa were carried out. For each isotherm, the system was automatically controlled and data were automatically acquired using home-made software, running under LabVIEW.

5.1.2 Frequency Measurements at Acoustic Resonances

Here, we describe our procedures for precisely determining the acoustic resonance frequencies of the gas-filled cavity, for static pressures ranging from 0.05 MPa to 0.7 MPa, at a temperature close to T_{TPW}.

For each mode, the source microphone was quickly stepped through 33 frequencies spanning the resonance to approximately determine the resonance frequency. The final resonance curve of the mode was obtained by averaging an increasing and a decreasing frequency sweep, as done in [1]. The resulting curve accounts for temperature changes during the measurements (drifts were less than $0.1\,\text{mK} \cdot \text{h}^{-1}$) and was interpolated as
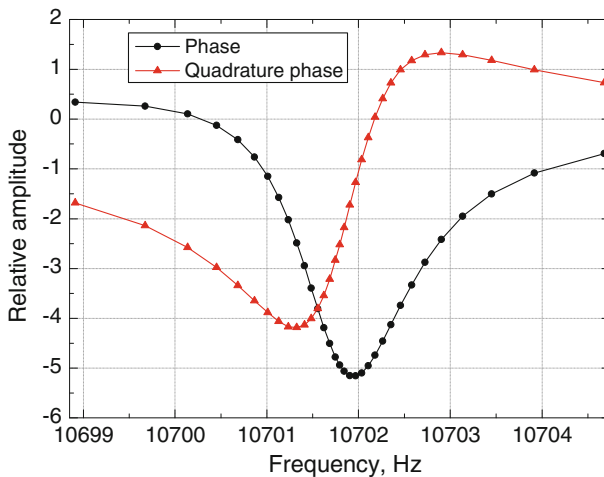

Fig. 18 Typical raw signals for the (0, 4) radial mode for argon at $p = 0.2\,\text{MPa}$. The *data points* correspond to the in-phase and out-of-phase signals from the lock-in, and the *solid line*s the computed signal magnitude

Fig. 19 Distribution of the 33 acoustic frequencies excited by a sweep around the resonance frequency of an acoustic mode. X is the signal in phase and Y is the quadrature component of the signal. The interval of frequencies around the resonance is chosen to get an equally spaced distribution in a Cartesian (X,Y) plot
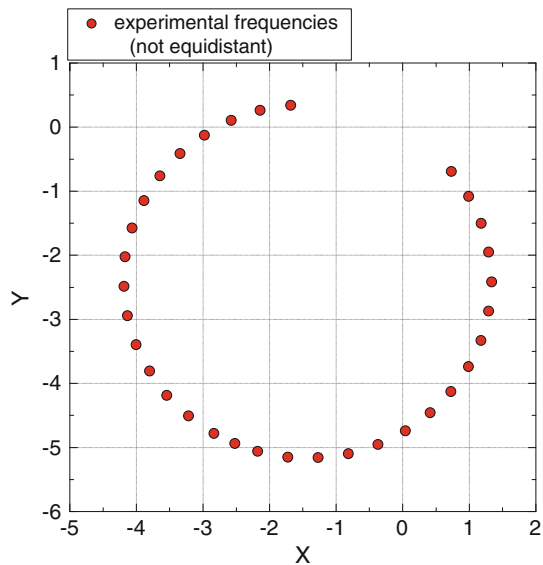
described in the next section. Figure 18 shows typical raw signals measured for the acoustic mode (0,4). The interval of frequencies around the resonance is chosen to get an equally spaced distribution in a Cartesian (X, Y) plot as shown in Fig. 19, where X is in-phase with the signal, and Y is the quadrature component of the signal. Typically, we needed 2 min to acquire data for each mode.

5.1.3 Fitting Method for Acoustic Data

The optimization method used for the interpolation of the frequency sweeps is the classic Levenberg-Marqardt method. The resonance function $V(f)$ fitted to the measured data is

$$V(f) = \frac{iAf}{\left(f^2 - F^2\right)} + B + C\,(f - f_{0n}) + D\,(f - f_{0n})^2 , \tag{5.1}$$

$$\text{with } F = f_{0n} + ig_{0n}\sqrt{f_{0n}/f} \tag{5.2}$$

where f is the source frequency, $V \equiv X + iY$ is the complex voltage detected by the lock-in amplifier, and f_{0n} and g_{0n} are the resonance frequency and the half-width that best fit the data. The function F in Eq. 5.2 differs from the traditional one ([1], named F' here)

$$F' = f_{0n} + ig_{0n} \tag{5.3}$$

We used the new form F instead of F' to account for the frequency-dependence of g_n that originates in the frequency-dependence of the thermoacoustic boundary layer. As demonstrated in [34], the change from F to F' changes the parameters f_{0n} and g_{0n}

Table 9 List of the different fit functions $V(f)$ and number of points used to estimate the parameters f_n and g_n

Function number	Fitting function type	No. of points
(1)	$V(f) = \dfrac{iAf}{\left(f^2-(f_{0n}+ig_{0n})^2\right)} + B + C(f - f_{0n})$	21
(2)	$V(f) = \dfrac{iAf}{\left(f^2-(f_{0n}+ig_{0n})^2\right)} + B + C(f - f_{0n})$	33
(3)	$V(f) = \dfrac{iAf}{\left(f^2-(f_{0n}+ig_{0n})^2\right)} + B + C(f - f_{0n}) + D(f - f_{0n})^2$	33
(4)	$V(f) = \dfrac{iAf}{\left(f^2-\left(f_{0n}+ig_{0n}\sqrt{f_{0n}/f}\right)^2\right)} + B + C(f - f_{0n}) + D(f - f_{0n})^2$	33

by terms of order $1/Q^2$, where Q is the quality factor of the resonance. In this work, the largest value of $1/Q^2$ was 4.04×10^{-8}, obtained with the mode (0,2) at 50 kPa; therefore, the change from F to F' might be significant. In order to detect any effect on k_B resulting from the choice of the function fitted to the acoustic resonance data, we analyzed the same acoustic data using the four fitting functions listed in Table 9. In Sect. 5.2.3, we show that the results using F are more consistent than the results using F'.

5.1.4 Acoustic Correction Model

In order to deduce the speed of sound (to determine k_B) and to test our understanding of the resonator from the measured resonance frequencies and half-widths, we need to apply corrections for small physical effects including the thermal boundary layers (TBL), bulk dissipation, the discontinuity of temperature between the gas and the wall, ducts, acoustic transducers, and the difference between the cavity's shape and a sphere. Each of these corrections can be estimated with well established models that are discussed elsewhere [10]. For example, the TBL corrections, bulk dissipation, and transducer corrections can be found in [2].

The only small change is our definition of the discontinuity of the temperature between the gas and the wall. In order to get the usual value of the thermal accommodation length l_{th} for argon at the temperature of the triple point of water T_{TPW}, $p = 0.1$ MPa and $h = 1$, $l_{th} = 118$ nm, we use this relation:

$$l_{th}(h) = \frac{\lambda}{p}\sqrt{\frac{\pi m T_{TPW}}{2k_B}}\frac{(2 - h)}{2h} \tag{5.4}$$

where λ is the thermal conductivity, m is the mass of an atom, h is the thermal accommodation coefficient, and p is the pressure. The difference is the factor 2 in the denominator, which was omitted in [15] and in [35].

Additional corrections are generated by the two capillary tubes that carry gas into and out of the QSR. These tubes are modeled as acoustic ducts that shift the resonance
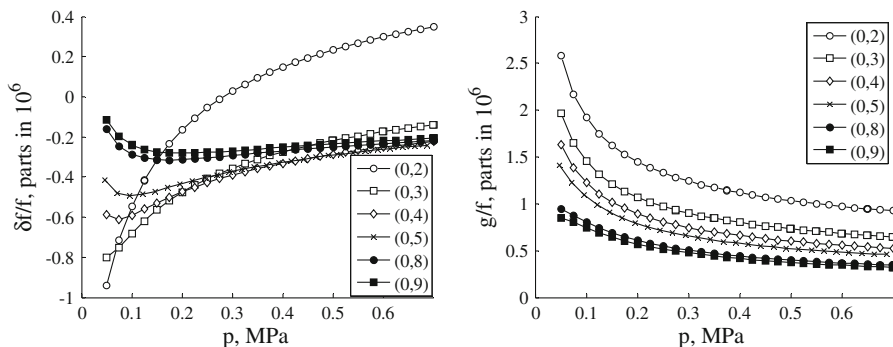
Fig. 20 Combined inlet and outlet duct frequency contributions on measurements of f_{0n} (*left*) and g_{0n} (*right*)
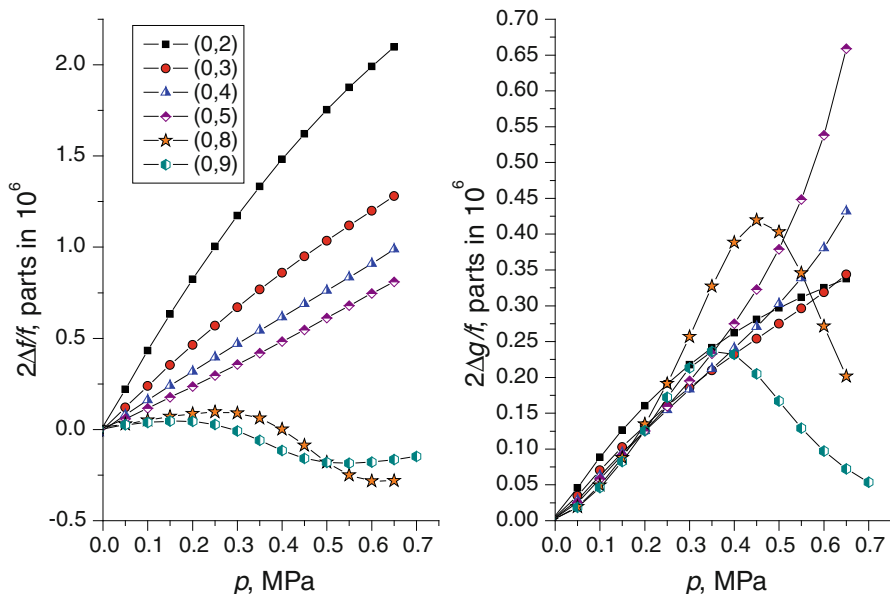

Fig. 21 Effect of the microphones on the frequencies (*left*) and on the half-widths (*right*) calculated using the model developed in [37] and [38]

frequencies and increase the losses. Corrections on the resonance frequency and the half-width were estimated by Mehl et al. [19] and have been tested by Gillis et al [36]. The inlet duct was composed of two tubes of lengths $l_{tube1} = 6\,\text{m}$ and $l_{tube2} = 0.05\,\text{m}$, and radii $r_{tube1} = 0.57\,\text{mm}$ and $r_{tube2} = 0.25\,\text{mm}$. The outlet duct was only one tube of length $l_{tube3} = 0.05\,\text{m}$ and $r_{tube3} = 0.38\,\text{mm}$. Figure 20 shows the calculated corrections, in parts in 10^6, to the resonance frequencies of a 0.5 L resonator generated by these ducts.

To calculate shifts in frequency and losses due to the two microphones, we used the model developed in [37] and [38]. As expected, the shifts depend on pressure and are

Table 10 Relative shape perturbations $10^6 \cdot \left(\left(k_{0n} \cdot a_{eq} \right)^2 - \left(Z_{0n}^A \right)^2 \right) \Big/ \left(Z_{0n}^A \right)^2$ to the eigenvalues of the first nine purely radial modes of BCU3

Radial acoustic mode $(0, n)$	BCU3 (microwave)	BCU3 (CMM)
(0, 2)	1.05	1.03
(0, 3)	3.10	3.09
(0, 4)	6.19	6.19
(0, 5)	10.30	10.31
(0, 6)	15.44	15.46
(0, 7)	21.60	21.63
(0, 8)	28.79	28.83
(0, 9)	37.01	37.07
(0, 10)	46.26	46.33

equal to zero at zero pressure. Figure 21 represents the frequency shifts (on the left) and the losses from the resonance frequencies (on the right) for the acoustic radial modes (0,2) through (0,5), and (0,8) and (0,9) generated by two 1/4 inch (6.35 mm) microphones, as calculated using the model in [38] under argon gas at 273.16 K.

Because the resonance frequencies were not measured exactly at T_{TPW}, they were corrected to T_{TPW}, as in [2] and [16].

Before fitting c_a^2 to a function of the pressure, we corrected the acoustic frequencies for the second-order shape perturbation. As shown above, our resonator BCU3 was a nearly perfect triaxial ellipsoid [19]. The shape perturbation was evaluated using the method of Mehl [39,40].

Data in Table 10 show the relative shape perturbation corrections $10^6 \cdot \left(\left(k_{0n} \cdot a_{eq} \right)^2 - \left(Z_{0n}^A \right)^2 \right) \Big/ \left(Z_{0n}^A \right)^2$ calculated by two independent methods, one using microwave data and the other using CMM data. Here, the term $(k_{0n} \cdot a_{eq})$ is the experimental determination of the eigenvalue associated with the wavenumber (0,n). The shape deformation parameters ε_1 and ε_2 from CMM measurements on BCU3 are taken from [23], and those from microwave measurements are indicated in Table 7.

We can also note that both values are compatible within their respective uncertainties. In Table 10 we can observe that the differences do not exceed 0.06 parts in 10^6, as in the case of the acoustic mode (0,9). This very small difference seems to indicate that our QSR BCU3 is a perfect triaxial ellipsoid.

With this last correction we have all the information to estimate c_a and then c_a^2.

The acoustic frequency measurements were repeated more than 15 times at each pressure. The standard deviation associated with the scatter of the 15 fitted values of f_{0n} was independent of the pressure and was of the order of 0.6 parts in 10^6, at least ten times larger than the fit uncertainty on each f_{0n} value. This surprised us because the quality factor Q of the resonances is a factor of three larger at 0.7 MPa than at 0.05 MPa and we expected the noise to be pressure-dependent as in [2]. The evaluations at zero pressure showed a constant dispersion as shown in Fig. 27. This implies that the noise did not originate in the electronics used to measure f_{0n}.

The measurements performed in [8] showed that the gas flow increased the uncertainty of the frequency measurements by more than a factor of two. We suspect that the same effect occurred during the present measurements. Consequently, and contrary to previous work [1,2,16], we did not apply pressure-dependent weights to our data when fitting c_a^2 to polynomial functions of the pressure. All the results presented here were deduced from *unweighted* fits.

We now discuss three additional, pressure-dependent phenomena that contribute to the interpretation of f_{0n}: the breathing motion of the shell, the thermal accommodation coefficient h, and the effects of gas flow in the QSR.

5.1.5 Breathing Motion of the Shell

The coupling between the shell's motion and acoustic resonances of the gas within the shell was investigated by Mehl [41] using the exact theory of elasticity of isotropic materials. The model predicts the frequency perturbations of the form:

$$\frac{\Delta f_{\text{shell}}}{f_{0n}} \approx \frac{\kappa p}{1 - (f_{0n}/f_{\text{shell}})^2} \tag{5.5}$$

where p is the pressure; f_{0n} is the unperturbed frequency of the nth radial acoustic mode; and f_{shell} is the frequency of one of the elastic modes of the empty shell which may or may not be a breathing mode. For the breathing mode of a spherical shell, κ is

$$\kappa = \frac{5a}{6t\rho_s c_L^2} \tag{5.6}$$

where t is the thickness of the shell, ρ_s is the density of the shell, and c_L is the longitudinal speed of sound in the shell. The resonator described in [1] behaved in reasonable agreement with Eqs. 5.5 and 5.6; however, the resonator described in [16] appeared to have a breathing frequency several kilohertz below the predicted frequency. We do not understand the relevant differences between these two resonators; therefore, we cannot trust Mehl's theory in the present work. Instead, we used the empirical method developed by Pitre et al. [16]. Pitre et al. replaced the constant κ in Eq. 5.6 with a function of the frequency that they deduced from their data. Here, we describe this approach in more detail.

Equation 5.5 predicts that the frequency perturbations generated by the shell's motion are approximately linear functions of the pressure. The perturbations are not exactly linear because the speed of sound in argon increases by 0.19 % when the pressure increases from 0.05 MPa to 0.7 MPa, and this pressure dependence affects the denominator of Eq. 5.5, $1 - (f_{0n}/f_{\text{shell}})^2$, especially when $f_{0n}/f_{\text{shell}} \approx 1$.

We used the linear approximation and we did not use the modes for which $|f_{0n}/f_{\text{shell}} - 1| < 0.02$. We followed the convention of representing the pressure dependence of the squared speed of sound with the acoustic virial expansion:

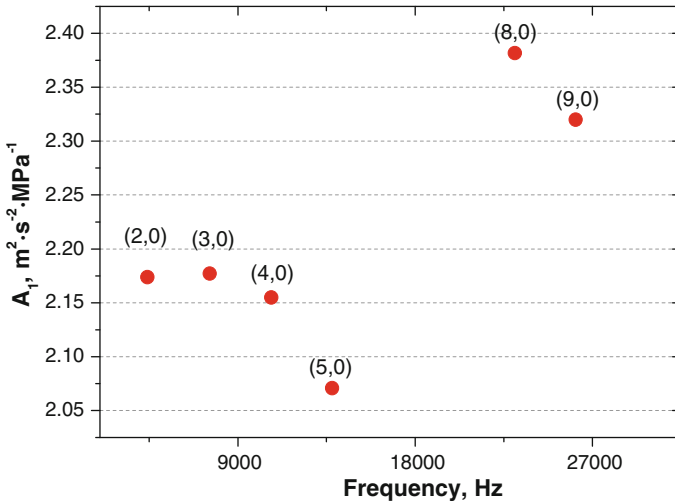$$c_a^2 - A_3 p^3 = A_0 + A_1 p + A_2 p^2 - A_{-1} p^{-1} \tag{5.7}$$

Fig. 22 Second acoustic virial coefficient A_1 as a function of the frequency of the $(0, n)$ acoustic modes

where the parameters A_0, A_1, A_2, and A_{-1} are fit to our data. A_0 represents the term independent of the pressure in Eq. 5.7, i.e., it corresponds to $\lim^*_{p \to 0} c_a^2 (p, T_{\text{TPW}})$ in Eq. 1.1.

Following [1], we used the literature value $A_3 = 1.45 \times 10^{-18} \, \text{m} \cdot \text{s}^{-2} \cdot \text{Pa}^{-3}$ [42] and, in our initial fitting, we set the thermal accommodation coefficient h in Eq. 5.4 exactly equal to 1, thereby fixing A_{-1}. In the linear approximation, the coefficient A_1 in Eq. 5.7 is the only coefficient affected by the shell's motion. Using the microwave values for $a_{\text{eq}}(p)$, we fitted Eq. 5.7 separately to the frequency data for each mode after correcting the frequency data for all known perturbations except for the interaction with the shell. Figure 22 displays the values of A_1 for six acoustic modes, as determined by this procedure.

We also measured the half-widths g_{0n} of the same six modes while cooling the resonator from $12\,^\circ\text{C}$ to $-4\,^\circ\text{C}$. We did not observe shell motion perturbations on modes $(0,2)$ through $(0,5)$ and $(0,8)$ and $(0,9)$.

We determined the parameters f_{shell} and κ in Eq. 5.5 for our shell by fitting the values of A_1 for the four modes $(0,2)$ through $(0,5)$ using the procedure of Pitre et al. [16] (described in detail by Sutton et al. [2]). The results were $\kappa = 2.53 \times 10^{-11} \, \text{Pa}^{-1}$ and $f_{\text{shell}} = 15.3 \, \text{kHz}$. To check these results, we calculated κ and f_{shell} using the dimensions of BCU3 and elastic properties of copper from the same billet that was used to make BCU3. (The elastic properties were measured at INRiM by S. Lago and P.A. Giuliano Albo during August 2009, and they are listed in Table 11). The calculated parameters were $\kappa = 2.14 \times 10^{-11} \, \text{Pa}^{-1}$ and $f_{\text{shell}} = 19.0 \, \text{kHz}$.

The disagreement between the fitted and calculated values of κ and f_{shell} is a measure of the difference between the real shell and Mehl's model shell. We interpret Eq. 5.5 as a physically motivated, empirical, perturbation function. We used this function with the fitted parameters to correct the frequency data before fitting Eq. 5.7 to determine the Boltzmann constant.

Table 11 Elastic properties of BCU3 copper measured at INRiM in January 2009

Property	Value	Relative uncertainty
Density ρ_s	$8\,916.1\,\text{kg} \cdot \text{m}^{-3}$	–
Longitudinal speed of sound c_L	$4\,668.2\,\text{m} \cdot \text{s}^{-1}$	0.16 %
Transverse speed of sound c_S	$2\,311.7\,\text{m} \cdot \text{s}^{-1}$	0.16 %
Young's modulus E	127.46 GPa	0.32 %
Shear modulus G	47.65 GPa	0.37 %
Bulk modulus K	130.77 GPa	0.54 %
Poisson's coefficient ν	0.338	0.29 %

5.1.6 Assessment of the Flow Effect

By July 2009 we had achieved such fine control of the temperature, pressure, flow, and gas purity, that we observed a flow dependence of the resonance frequencies. This phenomenon was not detected during previous speed-of-sound measurements because of higher noise levels [43]. Using both argon and helium, we studied the flow effect in an unsuccessful attempt to understand it quantitatively; however, we successfully constructed an empirical correlation to correct our data to zero flow.

The flow effect is independent of both the temperature of the gas and the acoustic mode studied [43]; therefore, we describe it using the symbol f_f to represent the frequency measured in BCU3 while gas was flowing. The fractional difference $\Delta f_f \equiv (f_f - f_{0n})/f_{0n}$ increases at low pressures [44]. As shown in Fig. 23 (left), $\Delta f_f = 1 \times 10^{-6}$ in argon at our lowest pressure (0.05 MPa) and highest flow 75 sccm[3]. In contrast, Δf_f decreased to approximately 0.4×10^{-6} at 0.4 MPa.

During July 2010, we conducted preliminary measurements of f_f in helium at the two static pressures of 0.2 MPa and 0.65 MPa (see Fig. 23, right.). At similar volumetric flows, the measured Δf_f values were almost the same at both pressures. In addition, the magnitude of the effect was considerably smaller in helium than in argon, and Δf_f was below 0.5×10^{-6}. We concluded that the flow effect can be considered constant in helium, independent of the flow rate applied in the resonator.

The complexity of the flow effect led us to model the gas flow inside the resonator using the commercial simulation software "COMSOL Multiphysics." As shown in Fig. 24, the model predicts that a gas jet flows out of the gas inlet tube, across the cavity, and then spreads across the wall opposite the inlet tube. These simulations were conducted for two flows (36 sccm and 60 sccm) well above the minimum in Δf_f at 10 sccm. Such jets are described in textbooks; however, we do not have a model for how the jet affects the frequencies of the radial acoustic modes.

---

[3] sccm = standard cubic centimeters per minute, corresponding to 1.6667×10^{-8} m$^3 \cdot$ s^{-1} in the International System of Units (SI). We define the volumetric flow 1 sccm as the flow of 1 cubic centimeter per minute of argon at the pressure 103 kPa and temperature 20 °C.
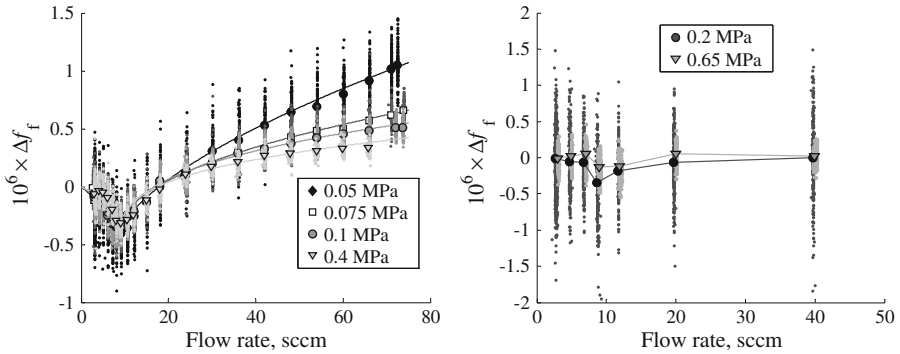
Fig. 23 *Left* Average values of the flow dependence on the resonance frequency measurements, as measured in argon using the (0, 3) mode of BCU3 at four static pressures. *Dots* represent experimental data and solid lines are fitting curves obtained with Eq. 5.8. *Right* Average values of flow-dependence on the resonant frequency measurements, as measured in helium using the (0, 3) mode of BCU3 at two static pressures. *Dots* correspond to experimental data. *Solid lines* do not represent fitted values
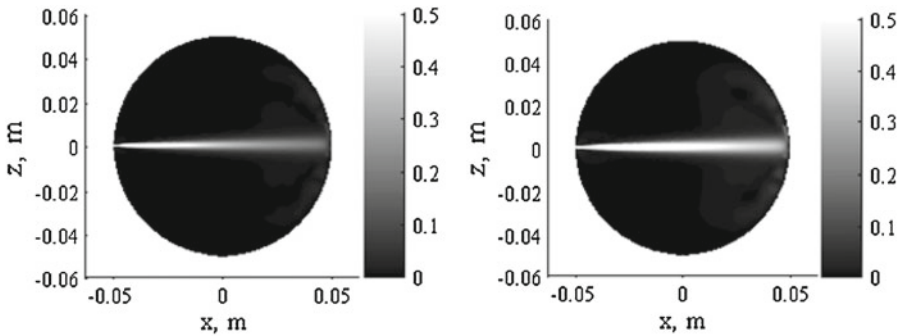
Fig. 24 Symmetrical slide of the inner flow velocity field estimation ($m \cdot s^{-1}$) obtained for two argon flows at 0.1 MPa: 36 sccm (*left*) and 60 sccm (*right*)

The flow effect was reproducible; therefore, we fitted the data in Fig. 23 (left) at each static pressure with the empirical function,

$$10^6 \cdot \Delta f_f = F_1 + F_2 \, |F_3 - \text{flow}|^{F_4} \tag{5.8}$$

where F_1, F_2, F_3, and F_4 were adjusted to fit the data at each static pressure and *flow* (expressed in sccm) is the flow measured at the flow controller, upstream of BCU3. Table 12 lists the resulting values of F_1, F_2, F_3, and F_4. The functional form, Eq. 5.8 does not have a physical meaning; however, it fits the data well and extrapolates to zero at zero flow.

Solid lines in Fig. 23 (left) represent the values Δf_f calculated at different static pressures with Eq. 5.8 and with the parameters provided in Table 12.

The coefficients F_1, F_2, F_3, and F_4 in Table 12 have smooth pressure dependences. To determine the speed of sound and the Boltzmann constant, we used Eq. 5.8 and the coefficients in Table 12 to correct every frequency measured with gas flowing to

Table 12 Fit parameters from the empirical function (Eq. 5.8): coefficients F_1, F_2, F_3, and F_4 values

Static pressure p (MPa)	F_1	F_2	F_3	F_4
0.050	−0.423(127)	0.212(073)	8.977(254)	0.631(077)
0.075	−0.420(198)	0.306(145)	8.764(371)	0.465(097)
0.100	−0.571(773)	0.575(191)	8.432(179)	0.324(061)
0.400	−0.510(698)	0.534(632)	8.793(443)	0.297(206)
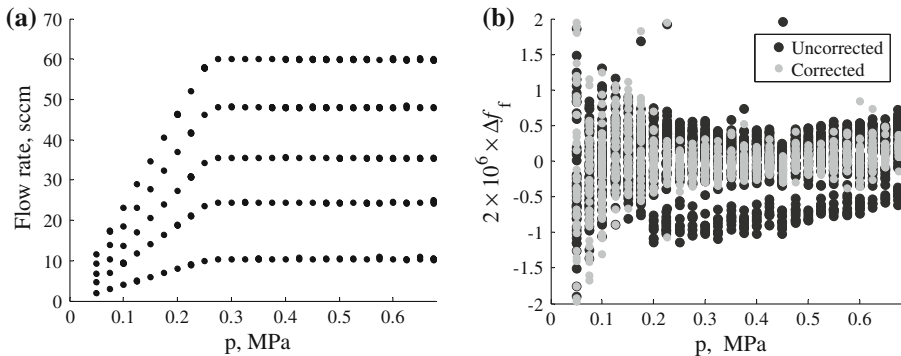
Fig. 25 (a) Gas flow rates realized during the July 2009 isotherm and (b) mode (0, 3) residuals before the gas flow correction (*black points*) and after the gas flow correction (*gray points*)

a zero-flow frequency. As shown in Fig. 25, this correction for the flow effect visibly improved the fit to the argon isotherm measured during July 2009.

5.1.7 Assessment of the Thermal Accommodation Coefficient h

The discontinuity of temperature between the gas and the wall is given by the term $(\gamma - 1)\, l_{th}/a_{eq}$[1], where l_{th} is defined in Eq. 5.4. We expect this correction to vary as p^{-1} and to have an identical value for each mode. In a first fit, we assumed that the thermal accommodation coefficient $h = 1$ and used it to estimate A_{-1} when fitting Eq. 5.7. After determining A_0 and A_{-1} in this approximation, we wrote

$$\frac{A_{-1}}{2 \cdot A_0} = \frac{(\gamma - 1)}{a_{eq}} l_{th}\,(h) - \frac{(\gamma - 1)}{a_{eq}} l_{th}\,(h = 1), \tag{5.9}$$

from which we obtained

$$h = \frac{\lambda\sqrt{\frac{\pi m T_{TPW}}{2k_B}} A_0\,(\gamma - 1)}{\lambda\sqrt{\frac{\pi m T_{TPW}}{2k_B}} A_0\,(\gamma - 1) + A_{-1} a_{eq}} \tag{5.10}$$

Table 13 Determination of the thermal accommodation coefficient h using Eq. 5.10 from fitted parameters A_{-1} and A_0 for modes (0, 2) to (0, 4)

Radial acoustic mode	A_0 (m$^2 \cdot$ s^{-2})	A_{-1} (m$^2 \cdot$ s$^{-2} \cdot$ Pa)	h
(0, 2)	94 755.956	0.017 8	0.77
(0, 3)	94 756.039	0.012 8	0.82
(0, 4)	94 756.018	0.016 9	0.78

to calculate the value of h for each acoustic mode. The values of h determined with Eq. 5.10 for each radial mode which is not perturbed by the shell resonance, are reported in Table 13.

The average of the tabulated values of h is 0.782, and the standard deviation is 0.025. We used the standard deviation as a measure of the uncertainty of the A_{-1} term.

5.1.8 Final Procedure for Fitting c^2

The last step of the data processing procedure was to correct all the data with the new estimate of h and to remove the gas flow effect with the corrections given in Sect. 5.1.6. Then, the corrected speed-of-sound data for each mode were fitted to two different functions of the pressure. The first function uses the equation,

$$c_a^2 - A_3 p^3 = A_0 + A_1 p + A_2 p^2 \qquad (5.11)$$

with the free parameters A_0, A_1, and A_2. The deviations from Eq. 5.11 for the modes (0,5) and (0,8) were large enough to be visually observable on the residual plot, but not exceeding 0.6 parts in 10^6, and had a curvature that we attribute to a perturbation from the motion of the shell. As explained in Sect. 5.1.5, the isolated-breathing-mode model does not accurately predict the frequency f_{shell} of the "breathing" mode of the copper quasi-spherical shells reported in [2,16], and [45], nor does it accurately predict f_{shell} of BCU3. In the case of BCU3, the prediction does not use data from the literature; instead, it uses the measured density, the Poisson ratio, and the longitudinal speed of sound of the copper that was used to build BCU3 [45]. If we assume that the (0,5) and (0,8) modes were close to elastic modes of the shell, the denominator of Eq. 5.5 might explain the deviations.

To test this assumption, we added to the function in Eq. 5.11 the term $A_3 p^3$ to form the new function given in Eq. 5.12 and we fitted the same data with it:

$$c_a^2 = A_0 + A_1 p + A_2 p^2 + A_3^* p^3 \qquad (5.12)$$

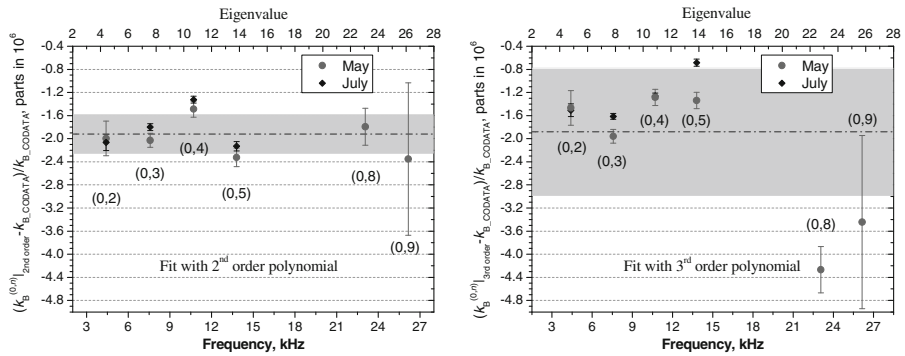where A_0, A_1, A_2, and A_3^* are free parameters.

Fig. 26 Final values of k_B determined by six modes in May 2009 and four modes in July 2009 plotted as fractional deviations from the CODATA value. The uncertainty bars represent the uncertainty of the parameter A_0 resulting from each fit. The values represented on the *left*, $k_B^{(0,n)}\big|_{\text{2nd order}}$, are determined with the second-order fitting function given in Eq. 5.11. The values on the right, $k_B^{(0,n)}\big|_{\text{3rd order}}$, are determined with the third-order fitting function given in Eq. 5.12. The *dashed gray lines* represent the average values $k_B|_{\text{2nd order}}$ (*left*) and $k_B|_{\text{3rd order}}$ (*right*), and the *gray areas* represent the uncertainties

5.2 Analyses of Isotherms and Discussion

5.2.1 Choice of the Fitting Function for the Speed-of-Sound Data

For each of the modes indicated, the left graph in Fig. 26 shows the relative difference between our determinations of the Boltzmann constant $k_B^{(0,n)}\big|_{\text{2nd order}}$ and the value currently published by the CODATA k_{B_CODATA}. Here $k_B^{(0,n)}\big|_{\text{2nd order}}$ represents the Boltzmann constant obtained from only one acoustic mode $(0, n)$, calculated with the second-order fit given in Eq. 5.11. The right graph in Fig. 26 shows the differences between $k_B^{(0,n)}\big|_{\text{3rd order}}$ and k_{B_CODATA}, where the values $k_B^{(0,n)}\big|_{\text{3rd order}}$ are computed using the third-order fitting polynomial given in Eq. 5.12.

In each graph of Fig. 26 we plot two sets of measurements; one set was conducted during May 2009 and used the modes (0,2), (0,3), (0,4), (0,5), (0,8), and (0,9); the second set was conducted during July 2009 and used the modes (0,2), (0,3), (0,4), and (0,5). Unfortunately, modes (0,8) and (0,9) in July were extremely noisy and unusable because of a power shortage and a software reset with a bad configuration. The differences plotted in Fig. 26 were obtained using the thermal accommodation coefficient h calculated as described in Sects. 5.1.4 and 5.1.7. The uncertainty bars on the experimental points in Fig. 26 represent the fitting uncertainty of the parameter A_0 of Eqs. 5.11 (left side) and 5.12 (right side).

The scatter of the values $k_B^{(0,n)}\big|_{\text{2nd order}}$ was 0.33 parts in 10^6, while it amounted to 1.1 parts in 10^6 for the values $k_B^{(0,n)}\big|_{\text{3rd order}}$. These uncertainties are represented with gray bands in Fig. 26. We explained this difference by the fact that we do not
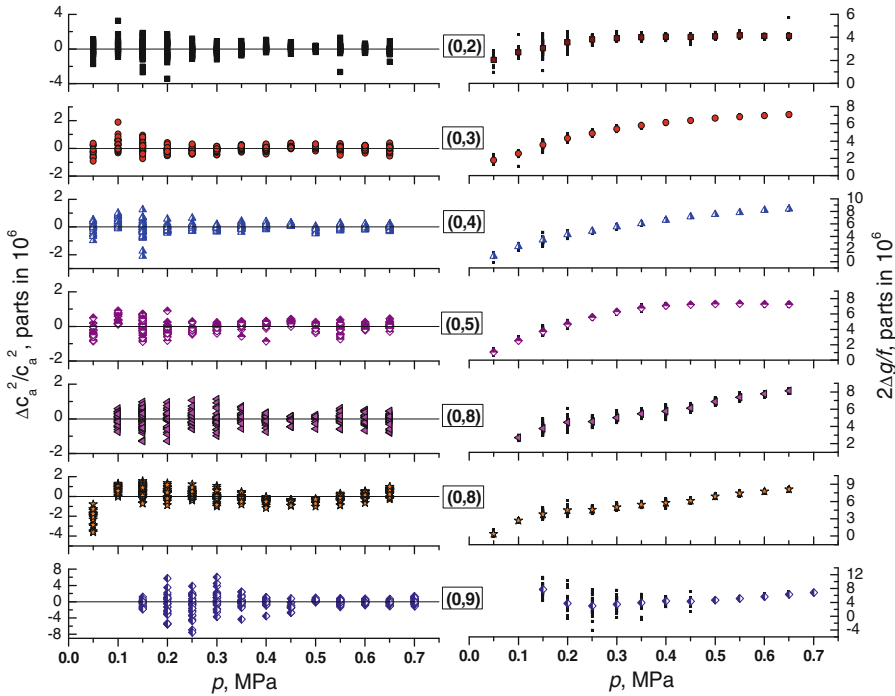
Fig. 27 Residuals (*left*) and excess half-widths multiplied by two (*right*) for the (0,2) to (0,9) modes, versus p isotherm. Mode (0,8) is plotted twice: the low pressure measurement at 0.05 MPa is represented only in the lower plot

dispose of an appropriate corrective model for the shell-motion effect. This introduces additional uncertainties affecting mostly the third-order fit, which is more sensitive to modelization errors. The effect was especially observable in the modes close to the shell mode, like the (0,5) and (0,8).

We calculated then the quantities $k_B|_{\text{2nd order}}$ and $k_B|_{\text{3rd order}}$, representing mean values obtained averaging the values $k_B^{(0,n)}\Big|_{\text{2nd order}}$ and $k_B^{(0,n)}\Big|_{\text{3rd order}}$, respectively. These two average values are represented with gray dashed lines in Fig. 26. $k_B|_{\text{2nd order}}$ and $k_B|_{\text{3rd order}}$ differed by only 0.04 parts in 10^6, but their difference was affected by an uncertainty of 1.15 parts in 10^6, mainly dominated by the effect of the scatter of the values $k_B^{(0,n)}\Big|_{\text{3rd order}}$.

All these elements led us to consider that the better estimate of k_B is given by $k_B|_{\text{2nd order}}$, and we decided to adopt $k_B \equiv k_B|_{\text{2nd order}}$ for the determination of the Boltzmann constant presented in this article.

We computed an unweighted average of the $k_B^{(0,n)}\Big|_{\text{2nd order}}$ values to obtain the final value of k_B. If we had computed a weighted mean using the uncertainties bars represented in the left graph of Fig. 26, only the modes (0,3), (0,4), and (0,5) would be taken into account because their uncertainties are five times smaller than those of the other points.

5.2.2 Excess of Half-Width

The *excess* of the half-width is the amount by which the measured half-width of a resonance exceeds that predicted by all of the effects discussed in Sect. 5.1. Therefore, the excess half-width is a measure of the size of the physical phenomena not included in our model for the acoustic resonator. Thus, the excess half-widths are an order-of-magnitude estimate of how our imperfect understanding of BCU3 affects our result for k_B. The excess half-width of each mode is plotted on the right-hand side of Fig. 27. These graphs represent the difference between the measured and the calculated half-widths; no empirical parameters were fitted to make these plots.

The extrapolations to zero pressure of twice the excess of the half-width of the modes (0,2), (0,3), (0,4), (0,5), and (0,8) are performed with a second-order polynomial and converge to an average value of 0.8 parts in 10^6 with a range from 0 parts in 10^6 to 1.3 parts in 10^6. This range is smaller than the value of 2.5 parts in 10^6 obtained by Moldover et al. in 1988 using a 3 L spherical resonator [1]. We have no explanation for the pressure dependences of the excess half-widths in Fig. 27; however, we are encouraged by the observation that all the excess half-widths are positive, in contrast with our earlier work reported in [2].

5.2.3 Fitting Acoustic Data with Different Combinations of Functions and Number of Data Points

In Sect. 5.1.3 and Table 9, we discussed four different combinations of functions (central column) and the number of data points (right column) that we used to determine f_{0n} and g_{0n} from the acoustic data. Figure 28 shows the sensitivity of the values of c_a^2 to the functions chosen to fit the acoustic data. Only small differences are observed: functions (3) and (4) in Table 9 generate nearly identical results while the results from function (1) have twice the uncertainty. The relative standard deviation for each mode has an average of 0.39 parts in 10^6. This small value shows that the different combinations of functions and number of data points are equivalent. The residuals from fitting function (2) were not random; therefore, this function was not used.

As we wrote above, we used only a linear pressure-dependence for the frequency perturbation from the motion of the shell (Eq. 5.8). Consequently, the values A_1, A_2, and A_3 of Eq. 5.11 and A_1, A_2, and A_3^* of Eq. 5.12 have a bias. The choice was also to use the value taken by [42] for A_3.

5.3 Uncertainty Budget for the Square of the Speed of Sound

We now summarize Sect. 5 to calculate the uncertainty budget for the acoustic measurements. Uncertainty values are expressed in terms of contributions to the square of the speed of sound c_a^2. The following sections describe how the different contributions are evaluated, and Table 14 provides the summary.
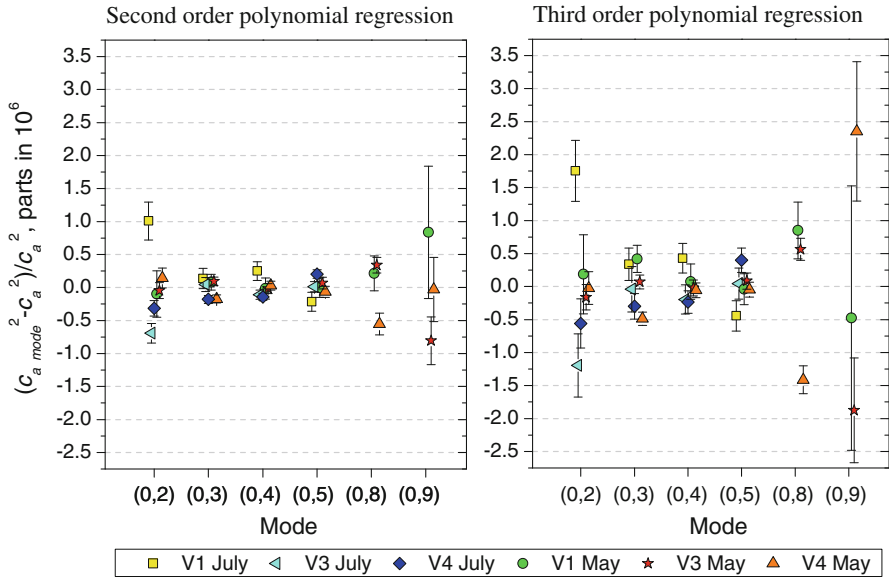
Fig. 28 *Left* Scatter of the zero-pressure extrapolations, performed with the second-order polynomial given in Eq. 5.11. V1, V3, and V4 indicate that f_n and g_n were calculated with the functions (1), (3), and (4) given in Table 9. *Right* Scatter of the zero-pressure extrapolations, performed with the third-order polynomial given in Eq. 5.12. Because the third-order polynomial has one more degree of freedom than the second-order polynomial, these results are more sensitive to noise than the results on the left

5.3.1 Scatter of Acoustic Measurements Among the Different Modes

This component accounts for the scatter among the results obtained from the acoustic modes from (0,2) to (0,5), (0,8), and (0,9) on the first isotherm, and (0,2) to (0,5) on the second isotherm discussed in Sect. 5.2.3. It was estimated by the use of the standard deviation over all the modes. Because imperfections in the model for the shape perturbation also contribute to the scatter among the modes; they are included in this component.

5.3.2 Thermal Accommodation

As mentioned in Sect. 5.1.7, we determined different values for the thermal accommodation coefficient h for the modes (0,2), (0,3), and (0,4).

We applied Eq. 5.10 to the data of the first isotherm and we calculated, for each mode, the thermal accommodation coefficient h, obtaining three different values with a standard deviation of ± 0.025. Then, we determined the thermal accommodation coefficient for the first isotherm as the average of these three values obtaining $h_{\text{isoth.1}} = 0.79$.

Using $h_{\text{isoth.1}}$ and the data of the first isotherm, we calculated the value of c_a^2 extrapolated at zero pressure, $c_a^2\big|_{h_{\text{isoth.1}}}$. To estimate the variation induced in c_a^2 by a change in h we calculated also $c_a^2\big|_{h_{\text{isoth.1}}+\delta h_{\text{isoth.1}}}$, where $\delta h_{\text{isoth.1}} =$

Table 14 Uncertainty budget associated with acoustic measurements for the determination of the Boltzmann constant

Term	Effect on k_B (parts in 10^6)	Note
Scatter among modes	0.35	Disagreement among modes (0, 2) to (0, 5), (0, 8), and (0, 9) modes for May 2009 isotherm and (0, 2) to (0, 5) modes for July 2009 isotherm. This includes the uncertainty on the shape perturbation, (Sect. 5.3.1)
Thermal conductivity of argon	0.02	As given in [46]
Accommodation coefficient dispersion	0.53	Effect of a dispersion of 0.026 on h, Sect. 5.3.2
Functional form of $c_a^2(p)$	0.39	Dispersion of the result according to function chosen
Shell perturbation	0.14	Difference in our result when we include a modified shell effect or not
A_3 uncertainty	0.07	Change from 1.30 to 1.45
Tubing acoustic impedance	0.23	Difference in our result when we increase the impedance by 10 %
Flow effect	0.11	10 % uncertainty on flow effect correction
Microphone impedance effect	0.05	Difference in our results when we consider the effect of microphone impedance
Pressure uncertainty	0.08	Offset of 100 Pa to explain the value of h
Total	0.80	Square root of the sum of squares

0.025 (the calculated standard deviation) and we found a relative difference $\left| \left(c_a^2 \big|_{h_{isoth.1}+\delta h_{isoth.1}} - c_a^2 \big|_{h_{isoth.1}} \right) \Big/ c_a^2 \big|_{h_{isoth.1}} \right| = 0.52 \times 10^{-6}$. This change represents an upper bound for the uncertainty component related to h, and it is included in our uncertainty budget.

Then, we applied Eq. 5.10 to the data of the second isotherm and we obtained $h_{isoth.2} = 0.812$. We calculated the value of c_a^2 extrapolated at zero pressure for the second isotherm, i.e. $c_a^2 \big|_{h_{isoth.2}}$ and we compared this value with $c_a^2 \big|_{h_{isoth.1}}$, obtaining a relative difference $\left| \left(c_a^2 \big|_{h_{isoth.2}} - c_a^2 \big|_{h_{isoth.1}} \right) \Big/ c_a^2 \big|_{h_{isoth.1}} \right| = 0.12 \times 10^{-6}$.

Considering that $h_{isoth.2} - h_{isoth.1} \approx \delta h_{isoth.1}$, we would have expected that $\left| \left(c_a^2 \big|_{h_{isoth.2}} - c_a^2 \big|_{h_{isoth.1}} \right) \Big/ c_a^2 \big|_{h_{isoth.1}} \right| \approx \left| \left(c_a^2 \big|_{h_{isoth.1}+\delta h_{isoth.1}} - c_a^2 \big|_{h_{isoth.1}} \right) \Big/ c_a^2 \big|_{h_{isoth.1}} \right|$, while this is not the case.

If the difference between $h_{isoth.2}$ and $h_{isoth.1}$ was attributable to a computational problem, the relative difference between $c_a^2 \big|_{h_{isoth.2}}$ and $c_a^2 \big|_{h_{isoth.1}}$ should have been of the order of 0.52×10^{-6}. The fact that $c_a^2 \big|_{h_{isoth.2}}$ and $c_a^2 \big|_{h_{isoth.1}}$ are instead so close can only be explained by the fact that the change in the thermal accommodation coefficient is due to a change that physically occurred in our experimental setup between the first and second isotherms. Moreover, the values found for $h_{isoth.2}$ and $h_{isoth.1}$ are

not in complete agreement with the value $h = 0.83$ measured in [2] for a particular, argon-filled copper resonator.

We found an explanation for that, and we consider that this is due to an error in the gas-pressure measurements corresponding to an offset of 100 Pa at 100 kPa in all the pressure sensors. This offset is relatively large but not impossible, as is shown also in [2], and its contribution is included in our budget of the uncertainties.

5.3.3 Thermal Conductivity of Argon

May et al. [46] measured the ratio (viscosity of argon)/(viscosity of helium) in the limit of zero density with the small fractional uncertainty of 0.00024. Using *ab initio* values for the Prandtl number [47], the viscosity of helium [47], and the pressure-dependence from [48], we deduced the value $\lambda^{Ar} = 16.419(4)\ \mathrm{mW \cdot m^{-1} \cdot K^{-1}}$ for the thermal conductivity of argon λ^{Ar} at 273.16 K and 0.1 MPa. If, in the future, a more accurate value for the thermal conductivity of argon is determined, our Boltzmann constant determination will change according to

$$\frac{\Delta k_{\mathrm{B}}}{k_{\mathrm{B}}} = 9.1 \times 10^{-5} \frac{\Delta \lambda}{\lambda} \tag{5.13}$$

Thus, the uncertainty of $0.004\ \mathrm{mW \cdot m^{-1} \cdot K^{-1}}$ of λ^{Ar} leads to an uncertainty of 0.02 parts in 10^6 in k_{B}.

5.3.4 Shell Motion Effect

The evaluation of the effect of the shell motion, a perturbation that has not been accurately modeled, is a challenge. As an alternative to our treatment in Sect. 5.1.5, we used Mehl's model [41] and we treated the thickness of the shell's wall and the longitudinal speed of sound as free parameters. In order to get those free parameters, we fit the difference between the present determination of the speed of sound and that reported in [1] using the modes (0,2) through (0,5), (0,8), and (0,9) simultaneously. From the fit, we obtained calculated values for both parameters 20 % higher than the measured ones. With these calculated parameters, the fractional difference between the present value of c_a^2 and that reported in [1] was only 0.14×10^{-6}. This difference is one estimate of the uncertainty contribution from the shell motion. This estimate is crude because the model for the shell motion is not accurate; however, the effect on c_a^2 is small, as expected, because the effect of the shell motion is a linear function of the pressure that vanishes at zero pressure.

5.3.5 Cubic Term in the Pressure A_3

As we wrote in Sect. 5.1.5, we corrected the shell perturbation effect using only a model linear in pressure (Eq. 5.5). The consequence is that the values A_1, A_2, A_3, and A_3^* of Eqs. 5.11 and 5.12 have a bias. At the same time, we used the value of Ewing and Goodwin for A_3 in [42], where they found two values, i.e., $1.45(2) \times 10^{-18}\ \mathrm{m^2 \cdot s^{-2} \cdot Pa^{-3}}$ and $1.51(4) \times 10^{-18}\ \mathrm{m^2 \cdot s^{-2} \cdot Pa^{-3}}$. Another reference [49]

gives $1.35(15) \times 10^{-18} \, \mathrm{m^2 \cdot s^{-2} \cdot Pa^{-3}}$. From those three independent values, we chose the weighted average value $A_3 = 1.45 \times 10^{-18} \, \mathrm{m^2 \cdot s^{-2} \cdot Pa^{-3}}$. We used the value $1.35 \times 10^{-18} \, \mathrm{m^2 \cdot s^{-2} \cdot Pa^{-3}}$ for uncertainty evaluation purposes only. The difference produced on our results with this change of the A_3 value is negligible within 0.07 parts in 10^6. Nevertheless, if in the future another experiment will estimate a better value of A_3, our k_B value will change according to the following equation:

$$\frac{\Delta k_B}{k_B} = -0.85 \times 10^{-6} \frac{\Delta A_3}{A_3} \tag{5.14}$$

5.3.6 Acoustic Impedance of Gas Ducts

Gillis et al. [36] tested the theory for the effects of gas ducts on the acoustic modes. They found agreement at the level of 1 % of the effects for long ducts and at the level of 10 % for short ducts. To be conservative, we added to our uncertainty budget the effect of a 10 % change in the acoustic admittance of the ducts. We note that our excess half-widths were positive and close to zero at low pressures. This suggests that there were no un-modelled acoustic losses in our apparatus at low pressures. Therefore the number 10 % is arbitrary. The impact on c_a^2 is 0.23×10^{-6}. This value is small because we chose the dimensions of our ducts to minimize their influence on the $(0, n)$ acoustic resonances [19].

5.3.7 Flow Effect

As described in Sect. 5.1.6, we applied an experimental correction on frequency measurements. At a given flow rate, we performed frequency measurements at several static pressures. Then, we corrected measurements with Eq. 5.8. The scatter of the corrected data was around 10 %, and we assumed that this was representative of the uncertainty associated with the flow correction. This uncertainty accounts for a Boltzmann constant uncertainty of 0.11 parts in 10^6.

5.3.8 Total Uncertainty Budget for Acoustic Measurements

The relative standard uncertainty of k_B related to the acoustic measurements is 0.80×10^{-6}, as detailed in Table 14.

From our analysis of A_0, we deduced also the square of the speed of sound, which was found to be $94\,755.988(117) \, \mathrm{m^2 \cdot s^{-2}}$.

6 Purity and Molar Mass of the Gas

In this section, we describe our efforts to characterize the purity of the gas used in our determination of the Boltzmann constant with the quasi-spherical resonator BCU3. We start with a description of the quality of our gas and then we discuss the gas-handling system and the purifier system. We conclude by estimating the contributions to the uncertainty of k_B related to the gas.

6.1 Gas Composition and Gas Handling System

The measurement of the speed of sound in the cavity is directly related to the molar mass of the gas $M_{Ar} = A_r(Ar) \cdot M_u$:

$$A_0(T) = \lim_{p \to 0}{}^{*} c_a^2(p, T) = \frac{5}{3}\frac{T N_A k_B}{A_r(Ar) \cdot M_u} \tag{6.1}$$

where $A_0(T)$ is the square of the speed of sound at zero pressure and at temperature T, $A_r(Ar)$ (or $A_r(^4He)$ in case helium is used instead of argon) is the relative atomic mass of argon (or helium), M_u is the molar mass constant, N_A is the Avogadro constant, and the factor 5/3 is the ratio $\gamma = C_p/C_V$ of the specific heat capacities for dilute monatomic gases.

6.1.1 Gas Composition

To accurately measure the Boltzmann constant (see Eq. 6.1), a very pure gas and a system to monitor and maintain this purity must be used. In this work, we used argon 6N Alphagaz, commercially available from Air Liquide. We sent a gas sample to the *Institute for Reference Material and Measurements* (IRMM)[4] of the European Joint Research Centre JRC to obtain an analysis of the relative abundances of the argon isotopes and an analysis of the chemical impurities in the gas. The methods used by IRMM are described in [50]. In Table 15, we report the IRMM analysis for the isotopic composition of our argon sample and for chemical impurities based on their mass spectrometry.

The gas sample sent to IRMM was collected from our gas handling system downstream from the acoustic resonator to ensure that the sample was representative of the gas that we used to measure the Boltzmann constant. The gas handling system is described in Sect. 6.1.2.

6.1.2 Gas Handling System and Gas Purification

In our apparatus, the manufacturer's gas cylinder was connected to a gas handling system used to purify the manufacturer's gas and to deliver it to the resonator at well-controlled pressures and flow rates. The feedback signal was given by the pressure transducer, and the stability of the pressure was of the order of 1 Pa. As already found in previous experiments described in [3], one of the limiting factors in acoustic measurements was related to pressure fluctuations during the flow control. By deliberately degrading the pressure stability by a factor of 2, we observed an increase in the acoustic noise by the same factor. The noise on the acoustic measurements was independent of the mode and the pressure (as show in Fig. 4 in [3]). As suggested by Michael

---

[4] European Commission Joint Research Centre, Institute for Reference Materials and Measurements, Retieseweg 111, B-2440, Geel, Belgium Tel.: +32 (0)14 571 211, Fax: +32 (0)14 584 273, http://www.irmm.jrc.be/.

Table 15 Gas composition

Gas properties		
Atomic mass[a] (10^{-3} kg · mol^{-1})		**Standard uncertainty on atomic mass[a] (10^{-3} kg · mol^{-1})**
M_{40}	39.962 383 123	0.003×10^{-6}
M_{36}	35.967 545 1	0.3×10^{-6}
M_{38}	37.962 732 4	0.4×10^{-6}
Total: M_{Ar}	39.947 805 1[b]	6.0×10^{-6} [c]
Isotopic ratios[d]		**Standard uncertainty on isotopic ratios[d]**
$r(^{36}Ar/^{40}Ar)$	0.003 346 0	1.5×10^{-6}
$r(^{38}Ar/^{40}Ar)$	0.000 634 77	0.26×10^{-6}
Impurities[d] (parts in 10^6)		**Standard uncertainty on impurities[d] (parts in 10^6)**
N_2	<2.00	2.00
O_2	<0.150	0.10
H_2O	<0.50	0.50
CO_2	<0.50	0.50
H_2	Not measured	Not measured
THC	Not measured	Not measured
He	<1.00	1.00
Ne	<1.00	1.00
Kr	Not measured	Not measured
Xe	Not measured	Not measured

[a] Values and uncertainties from CODATA 2006 [6]
[b] Calculated with Eq. 6.2
[c] Calculated with Eq. 6.3
[d] Measured by IRMM

Moldover[5], we suspect that the noise is originated by pressure fluctuations generated by the flow controller and transmitted adiabatically to the gas in the cavity.

Two different gas handling systems were constructed, one for argon and the other for helium. This prevented unintentional mixing of the two gases in the gas-handling system. Here, we focus on the argon gas handling system that delivered the argon used to determine the Boltzmann constant.

Both gas handling systems were assembled from electro-polished stainless steel tubes and all-metal pressure regulators to minimize gas absorption. Each gas handling system had a different purification stage, specifically developed for the type of gas used. The gas handling systems and the acoustic resonator were thoroughly cleaned by flowing pure gases through them for several years. Neither system was in contact with air for 3 years preceding the present measurements. The flowing gas diluted

---

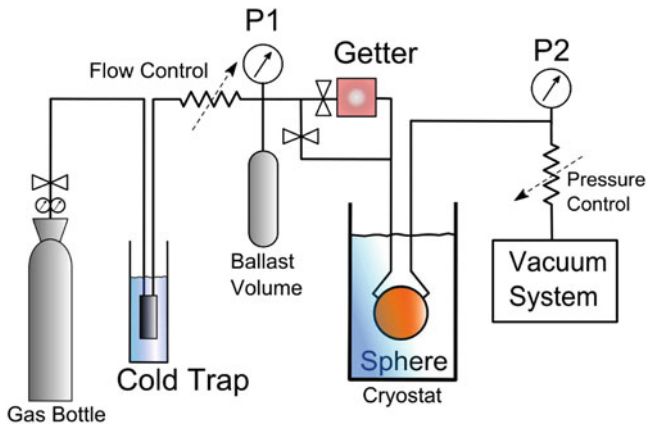5 Private communication from Michael Moldover, NIST.

Fig. 29 Schematic of the gas handling system

any outgassing impurities and, over time, may have possibly reduced the quantity of outgassing.

A schematic diagram of the argon gas handling system is shown in Fig. 29. The argon flowed from the manufacturer's cylinder through a cold trap at a temperature near 100 K. Flow and pressure control were regulated by mass flow controllers.

The getter was a Valco helium purifier (HP2). The manufacturer claimed that if the total concentration of impurities at the inlet were less than 10 parts in 10^6 by mole fraction, the concentration of impurities at the outlet would be less than 10 parts in 10^9 for H_2O, H_2, O_2, N_2, NO, NH_3, CO, CO_2, and CH_4. Other impurities removed include CF_4, CCl_4, SiH_4, and light hydrocarbons. The 100 K cold trap removes some noble gases such as Kr and Xe. This purification system cannot remove neon and helium from the argon because these noble gases do not react with the getter, and the temperature of the cold trap is too high to condense them.

During our argon measurements, we used flow rates ranging from 3 sccm to 80 sccm in order to detect possible outgassing in the sphere. No effects related to outgassing or the presence of water were observed. We emphasize that we made several microwave and acoustic tests that would have detected the effects of water described in [51]; however, we did not find such effects in our gas handling system.

To study the performance of the gas purification system, we monitored the variation of the difference between the temperature of the resonator measured by CSPRTs and the temperature deduced from acoustic measurements (see Eq. 6.1) for intervals of days. (see Fig. 30) During these intervals the getter and the cold trap were first deactivated and then reactivated. When both the cold trap and the getter were off, noise in the measured difference between the resistance and acoustic thermometers never exceeded 1×10^{-6} T_{TPW}. When the cold trap and the getter were turned on, we did not detect a change in either the temperature difference or the noise (see Fig. 30).

Figure 31 shows the Allan deviation σ of the difference between CSPRTs and acoustic temperature measurements, i.e., the square root of the Allan variance σ^2 [52]. The Allan variance is defined as one half the time average of the squares of the differ-
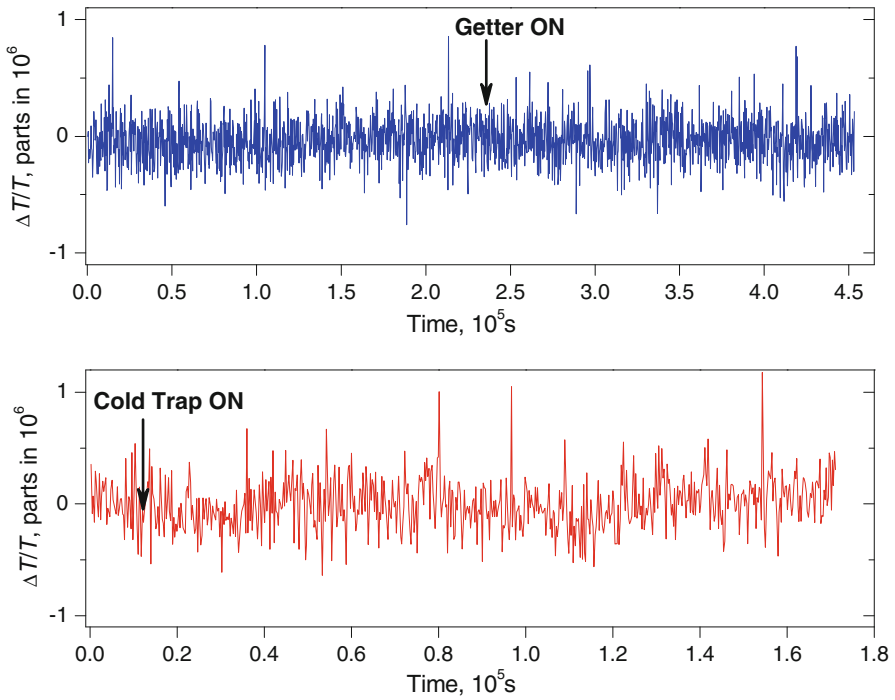
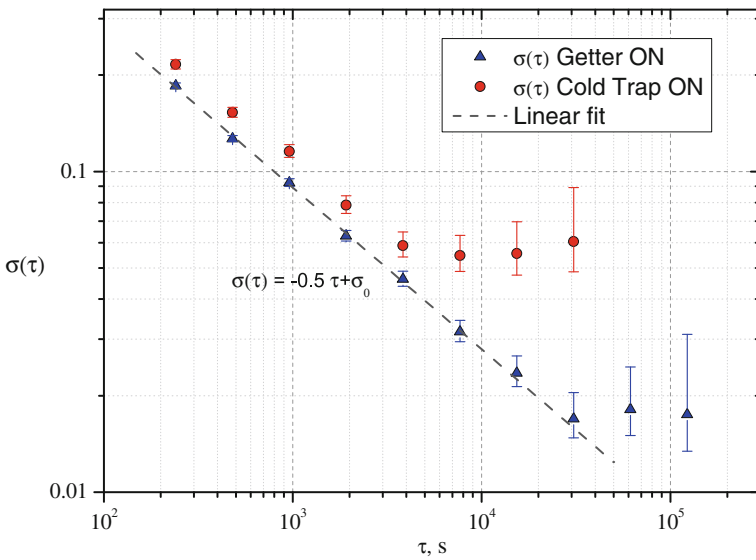**Fig. 30** Difference between CSPRT temperature and acoustic temperature

Fig. 31 Allan deviation of temperature difference between CSPRT temperature and acoustic temperature

ences between successive readings of the deviation, sampled over the sampling period τ (type N samples). It is intended to estimate the stability of noise processes. For white noise, the slope of the Allan deviation is $-1/2$. When the getter was turned on, a difference of -0.02×10^{-6} T_{TPW} (see Fig. 31) appeared between the acoustic and resistance thermometers at times $\tau > 10^4$ s. A larger difference (-0.12×10^{-6} T_{TPW}) appeared when we turned on the 100 K cold trap. We interpret these changes as indicating that the resonator's temperature did not change, but changes in the composition of the flowing gas changed the speed of sound, and therefore, the detected acoustic temperature. These measurements demonstrated the efficiency of our purification system and allowed us to estimate the amount of impurities present in the gas as it flowed through the resonator.

6.2 Determination of the Uncertainties Related to the Gas Composition

6.2.1 Uncertainties from Relative Isotopic Abundances and from Impurities Removed by the Getter and the Cold Trap

Here, we estimate the uncertainty of the atomic mass of the argon considering the contribution from the isotopic composition. In the following section, we consider helium and neon impurities.

The atomic mass of the argon is

$$M_{\text{Ar}} = A_{\text{r}}(\text{Ar}) \cdot M_{\text{u}} = \frac{M_{40}}{1 + r\left(\frac{^{36}\text{Ar}}{^{40}\text{Ar}}\right) + r\left(\frac{^{38}\text{Ar}}{^{40}\text{Ar}}\right)} + M_{36}\frac{r\left(\frac{^{36}\text{Ar}}{^{40}\text{Ar}}\right)}{1 + r\left(\frac{^{36}\text{Ar}}{^{40}\text{Ar}}\right) + r\left(\frac{^{38}\text{Ar}}{^{40}\text{Ar}}\right)}$$

$$+ M_{38}\frac{r\left(\frac{^{38}\text{Ar}}{^{40}\text{Ar}}\right)}{1 + r\left(\frac{^{36}\text{Ar}}{^{40}\text{Ar}}\right) + r\left(\frac{^{38}\text{Ar}}{^{40}\text{Ar}}\right)} \tag{6.2}$$

where $M_{40} = A_{\text{r}}(^{40}\text{Ar}) \cdot M_{\text{u}}$, $M_{36} = A_{\text{r}}(^{36}\text{Ar}) \cdot M_{\text{u}}$, and $M_{38} = A_r(^{38}\text{Ar}) \cdot M_{\text{u}}$. The ratios $r(^{36}\text{Ar}/^{40}\text{Ar})$ and $r(^{38}\text{Ar}/^{40}\text{Ar})$ are the fractions of the isotopes ^{36}Ar and ^{38}Ar, with respect to the most abundant isotope ^{40}Ar.

The associated uncertainty is

$$u\left(M_{\text{Ar}}\right)^2 = u\left(A_r(\text{Ar})\right)^2 \cdot M_{\text{u}}^2 = \frac{1}{\left(1 + r\left(\frac{^{36}\text{Ar}}{^{40}\text{Ar}}\right) + r\left(\frac{^{38}\text{Ar}}{^{40}\text{Ar}}\right)\right)^4} \cdot$$

$$\left(\left(\left(M_{40} - M_{38} - M_{38}r\left(\frac{^{36}\text{Ar}}{^{40}\text{Ar}}\right) + M_{36}r\left(\frac{^{36}\text{Ar}}{^{40}\text{Ar}}\right)\right)^2 u\left(r\left(\frac{^{38}\text{Ar}}{^{40}\text{Ar}}\right)\right)^2\right.$$

$$\left.+ \left(M_{40} - M_{36} - M_{36}r\left(\frac{^{38}\text{Ar}}{^{40}\text{Ar}}\right) + M_{38}r\left(\frac{^{38}\text{Ar}}{^{40}\text{Ar}}\right)\right)^2 u\left(r\left(\frac{^{36}\text{Ar}}{^{40}\text{Ar}}\right)\right)^2\right) \tag{6.3}$$

Table 16 Uncertainty budget due to noble gas impurities

Gas i	Relative atomic mass $A_r(i)$	Fraction in argon, x_i	$\Delta\ c_a^2\big|_{\text{mix(Ar}+i)}\Big/\ c_a^2\big|_{\text{Ar}}$
He	4.002 6035 2 [a]	2×10^{-6}	1.8×10^{-6}
Ne	20.179 7 [b]	2×10^{-6}	1.0×10^{-6}

[a] From [6]
[b] From [1]

Taking into account the values shown in Table 15, we found the value of $A_r(\text{Ar})$ for our gas sample. We calculated also the uncertainty contributions on k_B related to the isotopic composition, as well as those related to the impurities removed by the getter and the cold trap, i.e., all except helium and neon. The results are summarized in Table 17.

6.2.2 Uncertainties from Helium and Neon Impurities

We used the IRMM results (Table 15) to estimate an upper bound for the effect of helium and neon on the determination of the Boltzmann constant. This worst-case estimate assumes that the argon contained the mole fraction $x_{\text{He}} = 2 \times 0^{-6}$ of helium and the mole fraction $x_{\text{Ne}} = 2 \times 10^{-6}$ of neon. For helium, neon, and argon, the heat-capacity ratio is $\gamma \equiv C_P/C_V = 5/3$, in the limit of low pressure. For this special case, the expression for the speed of sound of a mixture reduces to $c_{\text{mix}}^2 = (5/3)\, k_B T / \sum_i x_i m_i$, where x_i is the mole fraction of the i-th component and m_i is the atomic mass of the i-th component [53].

Table 16 shows the relative change of c_a^2 due to the presence of either 2 parts in 10^6 of helium or 2 parts in 10^6 of neon in argon.

In our determination of the Boltzmann constant, we have considered that the best estimate for the relative molecular mass of the gas is the value $A_r(\text{Ar})$ that can be deduced from M_{Ar} in Table 15, and hence the most probable value of c_a^2 is actually $c_a^2\big|_{\text{Ar}}$, for the following reasons:

1. In similar measurements performed in the past [1,54], concentrations of neon and helium as high as the bounds in Table 15 were not observed. The NPL group intends to measure the presence of neon and helium at a detection level below 0.3×10^{-6}. To date, they have shown $x_{\text{Ne}} \leq 0.3 \times 10^{-6}$ [54].
2. Our experiments performed with the getter and the cold trap show that the impurity bounds provided by IRMM are overestimated by almost a factor of ten.
3. The argon is produced by an air liquefaction process, where helium and neon are present only in sub-part-per-million levels. During the production process, light impurities such as oxygen and nitrogen are removed; therefore, it is extremely plausible that most of the helium and neon are removed at the same time.

Because both helium and neon are lighter than argon, their presence in the argon can only reduce the molar mass of the mixture and increase its speed of sound. Thus, the speed of sound in the mixture is bound by the interval

Table 17 Uncertainty contributions from gas properties for determining the Boltzmann constant

Term	Relative standard uncertainty on k_B (parts in 10^6)	Notes
Isotopic composition	0.15	From IRMM measurements
Avogadro constant	0.05	From CODATA 2006
Getter Allan deviation	0.02	Change in composition of flowing gas due to the getter
Cold trap Allan deviation	0.06	Change in composition of flowing gas due to the cold trap
Subtotal (in quadrature)	0.16	Uncertainty on A_r (Ar)
Presence of He	0.52	From IRMM impurity measurements
Presence of Ne	0.29	From IRMM impurity measurements
Total	0.60	Total contribution (root sum of squares)

$\left[c_a^2 \big|_{\mathrm{Ar}} \; ; \; c_a^2 \big|_{\mathrm{Ar}} + \Delta\, c_a^2 \big|_{\mathrm{mix(Ar}+i)} \right]$. Since our best estimate of c_a^2 is $c_a^2 \big|_{\mathrm{Ar}}$, the uncertainty interval is asymmetric and corresponds to $\left[0 \; ; \; \Delta\, c_a^2 \big|_{\mathrm{mix(Ar}+i)} \right]$.

In the case of an asymmetric uncertainty interval, we can calculate the corresponding standard uncertainty following the equations given in Sect. 4.3.8 of [27]:

$$u\left(c_a^2 \big|_{\mathrm{Ar}} \right) = \sqrt{\frac{\left(\Delta\, c_a^2 \big|_{\mathrm{mix(Ar}+i)} - 0 \right)^2}{12}} = \sqrt{\frac{\left(c_a^2 \big|_{\mathrm{mix(Ar}+i)} - c_a^2 \big|_{\mathrm{Ar}} \right)^2}{12}} \qquad (6.4)$$

To summarize, we consider that the most appropriate value for the relative atomic mass of our argon is the value $A_r(\mathrm{Ar})$ that can be deduced from the value M_{Ar} provided in Table 15. We have collected new gas samples from our gas handling system and we have planned to send them to other laboratories, for an analysis of the presence of helium. We will publish a correction if any helium is found. The uncertainty values on k_B related to the presence of neon and helium in argon and calculated according to Eq. 6.4 are given in Table 17.

6.2.3 Total Uncertainty Budget for Gas Molar Mass

The uncertainty budget related to the evaluation of the molar mass of the argon is reported in Table 17. We expect to reduce this uncertainty in the near future by improving the analysis of the Ar gas, particularly for neon and helium.

7 Conclusion

We have reported on two sets of isothermal acoustic measurements carried out at LCM (LNE-CNAM) in a copper triaxial ellipsoid resonator of 0.5 L filled with argon, yielding a new determination of the Boltzmann constant. The average value for the

Boltzmann constant, with its associated combined standard uncertainty is

$$k_B = 1.380\ 647\ 74(171) \times 10^{-23}\ \text{J} \cdot \text{K}^{-1}.$$

The combined standard uncertainty corresponds to a relative combined standard uncertainty of 1.24 parts in 10^6.

Our value of k_B is 1.9 parts in 10^6 below the 2006 CODATA value [6] and it is consistent with it, within the combined standard uncertainties. (The fractional standard uncertainty of our value is 1.24×10^{-6}; the fractional standard uncertainty of the CODATA value is 1.7×10^{-6}).

The value for the universal gas constant R deduced from our measurement is $8.314\ 456\ 4(103)\ \text{J} \cdot \text{mol}^{-1} \cdot \text{K}^{-1}$.

With this measurement on a 0.5 L resonator, we have developed several new techniques and we have improved our knowledge of the existing theories and technologies. These advances, realized at LCM (LNE-CNAM) and by other research groups at NPL and INRIM [2,8,55], provide a further confirmation that the final aim of reducing the uncertainty of k_B below 1 part in 10^6 is likely to be achieved. We will apply this experience to future measurements using a 3.1 L quasi-spherical resonator. This will help in further reducing the uncertainty of the Boltzmann constant, to obtain a value suitable for the new definition of the kelvin.

References

1. M.R. Moldover, J.P.M. Trusler, T.J. Edwards, J.B. Mehl, R.S. Davis, J. Res. Natl. Bur. Stand. (U.S.) **93**, 85 (1988)
2. G. Sutton, R. Underwood, L. Pitre, M. De Podesta, S. Valkiers, Int. J. Thermophys. **31**, 1310 (2010)
3. L. Pitre, C. Guianvarc'h, F. Sparasci, A. Richard, D. Truong, Int. J. Thermophys. **29**, 1730 (2008)
4. Committee for Thermometry, Recommendation T2 to the CIPM, New Determinations of Thermodynamic Temperature and the Boltzmann Constant, *Working Documents of the 23rd Meeting of the Consultative Committee for Thermometry*, BIPM document CCT/05-31

5. J. Fischer, S. Gerasimov, K.D. Hill, G. Machin, M.R. Moldover, L. Pitre, P. Steur, M. Stock, O. Tamura, H. Ugur, D.R. White, I. Yang, Int. J. Thermophys. **28**, 1753 (2007)
6. P.J. Mohr, B.N. Taylor, D.B. Newell, Rev. Mod. Phys. **80**, 633 (2008)
7. L. Pitre, C. Guianvarc'h, F. Sparasci, A. Guillou, D. Truong, Y. Hermier, M.E. Himbert, C. R. Phys. **10**, 835 (2009)
8. R.M. Gavioso, G. Benedetto, P.A. Giuliano Albo, D. Madonna Ripa, A. Merlone, C. Guianvarc'h, F. Moro, R. Cuccaro, Metrologia **47**, 387 (2010)
9. J.T. Zhang, H. Lin, X.J. Feng, J.P. Sun, K.A. Gillis, M.R. Moldover, Y.Y. Duan, Int. J. Thermophys. doi:10.1007/s10765-011-1001-3
10. C. Guianvarc'h , L. Pitre, M. Bruneau, A.-M. Bruneau, J. Acoust. Soc. Am. **125**, 1416 (2009)
11. M.R. Moldover, J.B. Mehl, M. Greenspan, J. Acoust. Soc. Am. **79**, 253 (1986)
12. J.B. Mehl, M.R. Moldover, Phys. Rev. A **34**, 3341 (1986)
13. M.R. Moldover, S.J. Boyes, C.W. Meyer, A.R.H. Goodwin, J. Res. Natl. Inst. Stand. Technol. **104**, 11 (1999)
14. M.B. Ewing, J.P.M. Trusler, J. Chem. Thermodyn. **32**, 1229 (2000)
15. G. Benedetto, R.M. Gavioso, R. Spagnolo, P. Marcarino, A. Merlone, Metrologia **41**, 74 (2004)
16. L. Pitre, M.R. Moldover, W.L. Tew, Metrologia **43**, 142 (2006)
17. D.C. Ripple, G.F. Strouse, M.R. Moldover, Int. J. Thermophys. **28**, 1789 (2007)
18. R.M. Gavioso, D. Madonna Ripa, C. Guianvarc'h, G. Benedetto, P.A. Giuliano Albo, R. Cuccaro, L. Pitre, D. Truong, Int. J. Thermophys. **31**, 1739 (2010)
19. J.B. Mehl, M.R. Moldover, L. Pitre, Metrologia **41**, 295 (2004)
20. E.F. May, L. Pitre, J.B. Mehl, M.R. Moldover, J.W. Schmidt, Rev. Sci. Instrum. **75**, 3307 (2004)
21. J.B. Mehl, Metrologia **46**, 554 (2009)
22. R.J. Underwood, J.B. Mehl, L. Pitre, G. Edwards, G. Sutton, M. de Podesta, Meas. Sci. Technol. **21**, 075103 (2010)
23. M. de Podesta, E.F. May, J.B. Mehl, L. Pitre, R.M. Gavioso, G. Benedetto, P.A. Giuliano Albo, D. Truong, D. Flack, Metrologia **47**, 588 (2010)
24. P.A. Giuliano Albo, INRIM, private note
25. R. Underwood , D. Flack, P. Morantz, G. Sutton, P. Shore, M. de Podesta, Metrologia **48**, 1 (2011)
26. Supplementary Information for the International Temperature Scale of 1990, BIPM (1997), http://www.bipm.org
27. Evaluation of measurement data—Guide to the expression of uncertainty in measurement, GUM 1995 with minor corrections, JCGM 100:2008, First edn. (JCGM, 2008)
28. T.J. Buckley, J. Hamelin, M.R. Moldover, Rev. Sci. Instrum. **71**, 2914 (2000)
29. J.B. Mehl, private communication
30. J.D. Jackson, *Classical Electrodynamics*, 3rd edn. (Wiley, New York, 1999)
31. R.M. Gavioso, G. Benedetto, D. Madonna Ripa, P.A. Giuliano Albo, C. Guianvarc'h, A. Merlone, L. Pitre, D. Truong, F. Moro, R. Cuccaro, Progress in INRiM experiment for the determination of the Boltzmann constant with a quasi-spherical resonator. Int. J. Thermophys., doi:10.1007/s10765-011-1032-9.
32. D.C. Ripple, D.R. Defibaugh, K.A. Gillis, M.R. Moldover, in *Proceedings of TEMPMEKO'99, 7th International Symposium on Temperature and Thermal Measurements in Industry and Science*, ed. by J. F. Dubbeldam, M.J. de Groot (Edauw Johannissen bv, Delft, 1999), pp. 418–423
33. D.C. Ripple, G.F. Strouse, M.R. Moldover, Int. J. Thermophys. **28**, 1789 (2007)
34. K.A. Gillis, I.I. Shinder, M.R. Moldover, Phys. Rev. E **70**, 021201 (2004)
35. M.R. Moldover, Comptes Rendus Physique **10**, 815 (2009)
36. K.A. Gillis, H. Lin, M.R. Moldover, J. Res. Natl. Inst. Stand. Technol. **114**, 263 (2009)
37. C. Guianvarc'h, R.M. Gavioso, G. Benedetto, L. Pitre, M. Bruneau, Rev. Sci. Instrum. **80**, 074901 (2009)
38. M. Bruneau, A.-M. Bruneau , Z. Škvor, P. Lotton, Acta. Acoust. **2**, 223 (1994)
39. J.B. Mehl, J. Res. Natl. Inst. Stand. Technol. **112**, 163 (2007)
40. J.B. Mehl, Int. J. Thermophys. **31**, 1259 (2010)
41. J.B. Mehl, J. Acoust. Soc. Am. **72**, 782 (1985)
42. M.B. Ewing, A.R.H. Goodwin, J. Chem. Thermodyn. **24**, 531 (1992)
43. A. Guillou, L. Pitre, D. Truong, F. Sparasci, C. Guianvarc'h, BCU2V2 (2007) to BCU3 (2009): the improvements made in our last apparatus for the Boltzmann's constant redetermination with an acous-

tic method, *IV International Workshop on Progress in Determining the Boltzmann Constant*, Turin, Italy (2009), http://www.inrim.it/kb2009

44. A. Guillou, L. Pitre, F. Sparasci, D. Truong, New determination of the Boltzmann constant with an acoustic quasi spherical resonator filled with argon, *EAA EUROREGIO on Sound and Vibration*, Ljubljana, Slovenia (2010)
45. D. Truong, F. Sparasci, E. Foltête, M. Ouisse, L. Pitre, Int. J. Thermophys. **32**, 427 (2011)
46. E.F. May, M.R. Moldover, R.F. Berg, J.J. Hurly, Metrologia **43**, 247 (2006)
47. J.J. Hurly, J.B. Mehl, J. Res. Natl. Inst. Stand. Technol. **112**, 75 (2007)
48. G.C. Maitland, R. Rigby, E.B. Smith, W.A. Wakeham, *Intermolecular Forces: Their Origin and Determination* (Clarendon Press, Oxford, 1981), pp. 568–572
49. A.F. Estrada-Alexanders, J.P.M. Trusler, J. Chem. Thermodyn. **27**, 1075 (1995)
50. S. Valkiers, D. Vendelbo, M. Berglund, M. de Podesta, Int. J. Mass Spectrom. **291**, 41 (2010)
51. M. de Podesta, G. Sutton, R. Underwood, S. Bell, M. Stevens, T. Byrne, P. Josephs-Franks, Metrologia **48**, L1 (2010)
52. D.W. Allan, IEEE Trans. Ultrason. Ferroelectr. Freq. Control **34**, 647 (1987)
53. W. Van Dael, in *Experimental Thermodynamics, Volume II. Experimental Thermodynamics of Non-reacting Fluids*, ed. by B. Le Neindré, B. Vodar (Butterworths, London, 1975)
54. M. de Podesta, G. Sutton, R. Underwood, M. Perkin, S. Davidson, P. Morantz, Int. J. Thermophys. **32**, 413 (2011)
55. L. Pitre, A. Guillou, D. Truong, F. Sparasci, C. Guianvarc'h, An acoustic/microwave determination of the Boltzmann constant at LNE-INM/CNAM, Presented at *the IV International Workshop on Progress in Determining the Boltzmann Constant*, Torino, Italy (2009), http://www.inrim.it/kb2009